Counting What Can Be Counted: Evaluating the Limits of LEEM-EDX

Sohl, Bernard

Counting What Can Be Counted: Evaluating the Limits of LEEM-EDX

THESIS

submitted in partial fulfillment of the
requirements for the degree of

MASTER OF SCIENCE
in
PHYSICS

Author :	Bernard Sohl
Student ID :	2598914
Supervisor :	Prof. dr. Ir. S.J. van der Molen
Second corrector :	Dr. M.P. Allan

Leiden, The Netherlands, August 27, 2025

Counting What Can Be Counted: Evaluating the Limits of LEEM-EDX

Bernard Sohl

Huygens-Kamerlingh Onnes Laboratory, Leiden University
P.O. Box 9500, 2300 RA Leiden, The Netherlands

August 27, 2025

Abstract

This thesis evaluates the capabilities and detection limits of the energy-dispersive X-ray spectroscopy (EDX) system integrated into the ESCHER low-energy electron microscope (LEEM) for compositional analysis of in-situ grown thin-film Cs_3Sb photocathodes. The project aimed to assess whether the photocathodes grown in the system exhibit stoichiometries consistent with expectations and to determine whether the LEEM-EDX setup can reliably measure them. Two complementary analysis methods, matrix-corrected least-squares (MLLSQ) fitting with standard-based quantification and Monte Carlo simulations of X-ray generation, were both implemented in DTSA-II and applied to photocathodes of varying thickness. The results show that typical thin-film photocathodes are near the detection limit of the system, making reliable quantification difficult, while thicker samples yield more distinct compositional information and more representative ratios. Although the findings indicate the photocathodes are approximately within the expected stoichiometric range, the current limitations of the setup prevent definite conclusions.

Contents

Version of August 27, 2025– Created August 27, 2025 - 11:10

Chapter 1

Introduction

Energy-Dispersive X-ray Spectroscopy (EDX) is an analytical technique that performs elemental analysis or chemical characterization. It relies on detecting characteristic X-rays emitted from a material when it is excited by an electron beam, making it a form of emission spectroscopy. Since the start of its development in the 1950s, EDX has become a valuable tool in material science, particularly when combined with electron optics. The origins of EDX lie in the first use of gas-filled proportional counters for detecting X-rays in 1954 by Arndt et al. [5], which relied on the X-ray emission from the sample exiting a gas-filled chamber, where it ionized the gas and generated a measurable electrical signal. Although the resolution was typically limited to around 1.3 to 1.8 keV, these proportional counters showed significant promise and found practical use in other applications. Notably, X-ray fluorescence spectrometers based on similar detectors were included on the Viking landers that explored Mars, where they analyzed the Martian soil [10].

In 1966, Bowman et al. initiated an important development by publishing a paper on the use of lithium-drifted silicon (Si(Li)) solid-state detectors. These detectors were originally intended for γ-ray detection, a task in which they excelled. However, they also showed promising results in the X-ray energy range, achieving an energy resolution of around 1.1 keV [9]. This led Fitzgerald et al. to develop a specialized Si(Li) X-ray spectrometer for use in electron probe microanalyzers, which initially had a resolution of 600 eV but was quickly improved to around 200 eV, achieving X-ray photon count rates of up to 25,000 counts per second [11]. This advancement established solid-state energy-dispersive X-ray spectroscopy as a widely adopted technique for both quantitative and qual-

itative analysis of X-ray spectra across various electron and X-ray-based measurement instruments. The technique has undergone significant improvements since its early development in the 1960s and remains a cornerstone of material analysis today. Modern EDX systems have transitioned to silicon drift detectors (SDDs), achieving energy resolutions as low as 122 eV and counting rates exceeding 1,000,000 counts per second.

While EDX has long been a widely used technique in instruments such as X-ray fluorescence (XRF) spectrometers, scanning electron microscopes (SEM), and transmission electron microscopes (TEM), its integration into electron microscopes is particularly convenient, as the same electron beam used for imaging can be used for an EDX measurement. Allowing for simultaneous spatial imaging and EDX measurements.

1.1 Background and Motivation

At the van der Molen research group, where this project was carried out, most research is conducted using a Low-Energy Electron Microscope (LEEM). In a LEEM, low-energy electrons are utilized to image surfaces with high spatial resolution while minimizing sample damage. At these energies, it can also provide valuable information about the materials' electronic structure and surface morphology, making it an ideal technique for studying thin films and surface phenomena.

Until recently, EDX had not been implemented in a LEEM system [26]. This is primarily because LEEM operates with very low-energy electrons for imaging, typically in the range of 0-100 eV, which is insufficient to excite inner-core electrons and thus generate characteristic X-rays. It is generally accepted that incident electrons must have energies of at least 5 keV to perform meaningful EDX measurements. As a result, unlike other EDX-capable electron imaging techniques, LEEM cannot perform imaging and EDX analysis simultaneously under standard operating conditions. In-situ compositional analysis was therefore not considered a necessity in LEEM setups, and could be carried out on a different instrument before measurements. However, this is not always practical, particularly in cases where the sample may degrade or be too fragile during transfer to or from the LEEM system.

ONEM

This became a relevant problem with the development of Optical Near-Field Electron Microscopy (ONEM) in the van der Molen group. ONEM is a novel imaging technique in which the non-invasive imaging capabilities of light and the high spatial resolution of electron microscopy are combined. In ONEM, the sample is illuminated with visible light, and the resulting near-field light distribution is converted into an electron flux by a thin photocathode layer. This electron signal, which retains the spatial information of the optical near field, is then imaged using the LEEM optics. By capturing light in the near-field regime, ONEM avoids diffraction-induced blurring and allows optical features below the classical resolution limit to be imaged, effectively making it a super-resolution technique. ONEM can be used to study samples such as thin films, lithographed patterns, and even samples suspended in liquid using a special sample holder. This makes it possible to image biological samples or electrochemical processes and even plasmonic phenomena [23].

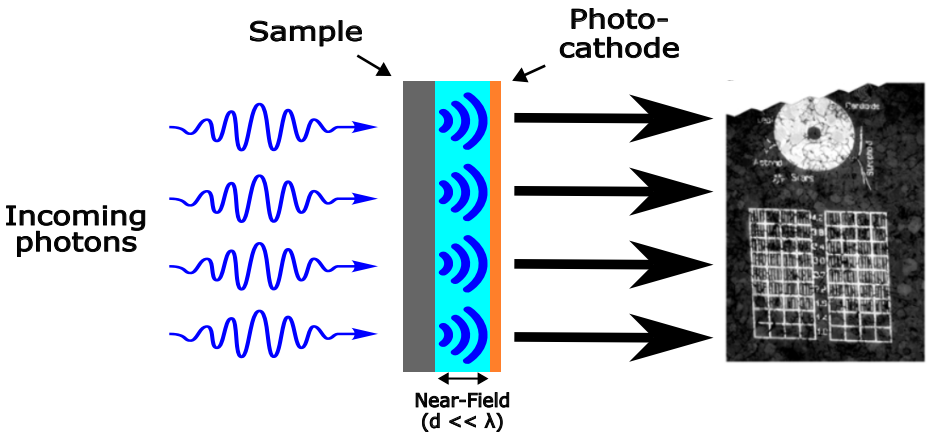

Figure 1.1: *Illustration of the working principle of ONEM. Light interacts with the sample and is converted in the optical near-field into a spatially varying electron flux by a photocathode layer. This electron image, which retains sub-wavelength detail, is then projected using LEEM optics (own work).*

One of the main challenges of ONEM is the successful fabrication and implementation of high-quality photocathodes. These photocathodes are very thin photosensitive layers that turn photons into electrons. One of the Photocathodes used for ONEM research is cesium-antimonide (Cs_3Sb). These photocathodes must be grown in situ to ensure cleanliness and sta-

bility, as they are very reactive and degrade quickly in exposure to the atmosphere, which poses a big challenge when evaluating their properties after growth. A crucial limitation as the performance of the photocathodes depends significantly on their stoichiometry, purity, and thickness. The LEEM optics cannot measure these properties, so at the time, there was no method to perform in-situ compositional analysis of samples.

This changed with the work of Rudolf Tromp and Joshua Schaafsma, who built an EDX setup into the LEEM through relatively straightforward modifications. Tromp wrote an article in *Ultramicroscopy* about the project, showing that high-quality X-ray spectra could be acquired from a range of samples, thereby enabling elemental analysis in LEEM for the first time [26]. While Joshua conducted a more extensive implementation and optimization study as part of his bachelor's thesis, focusing on detector calibration, data correction methods, and preliminary measurements on various materials [19]. Their combined work served as a strong proof of concept, demonstrating the capabilities of the EDX in the LEEM system. Joshua's work laid the groundwork for stoichiometric analysis and quantitative analysis in this system, forming the basis on which this project builds.

1.2 Objectives and Scope of the Thesis

The main objective of this project is to develop a robust procedure for quantitative compositional analysis of samples in the LEEM system using EDX. This involves obtaining quantitative information about a sample's composition (stoichiometry) and thickness. This proved to be quite a challenge due to the unique constraints, electron beam properties, and geometry of the LEEM system. Moreover, unlike traditional SEM and TEM-based EDX setups, the lack of commercial hardware and software solutions for EDX in LEEM requires a custom method tailored specifically to this system. This custom method includes implementing calibration standards, universal spectrum analysis software, simulation tools, and a dedicated analysis workflow. This project aims to establish a reproducible method for determining the stoichiometry and thickness of in-situ grown photocathodes, which are central to optimizing ONEM performance. In particular, this involves demonstrating reliable quantification of Cs and Sb, creating standards which can be used for future stoichiometric analysis, and verifying the approach by comparison with simulations.

Chapter 2

Theory

This chapter provides the theoretical background necessary to understand this project. LEEM is an electron microscopy technique whose strengths and limitations directly affect how techniques like EDX can be used. ONEM builds on LEEM by introducing a thin photocathode layer to convert photons into electrons. The quality and composition of this layer are critical but not easily measured directly. This chapter outlines the key principles of LEEM, ONEM, and photocathodes, followed by the principles of EDX and how it can be used for quantitative analysis of the system.

2.1 Low Energy Electron Microscopy

Low Energy Electron Microscopy (LEEM) is a surface-sensitive imaging technique that uses low-energy electrons (typically 0-10 eV) to probe the structural and electronic properties of sample surfaces. While the Introduction gave a general overview of its role in this project, here we focus on the underlying physics principles essential for understanding LEEM.

The primary instrument used in this work is an aberration-corrected low-energy electron and photoemission electron microscope, known as the ESCHER LEEM. Although it supports both LEEM and PEEM, neither was directly used here. The system features an electrostatic mirror that corrects chromatic and spherical aberrations, improving resolution from 4.1 nm to about 2 nm [25]. The following sections describe the key components of the LEEM system in the order electrons pass through them, as shown in Figure 2.1.

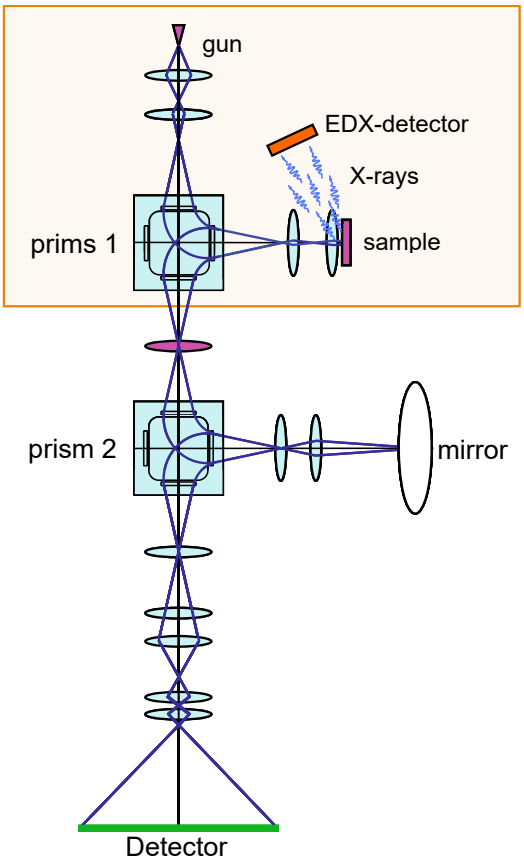

Figure 2.1: *A schematic of the ESCHER LEEM with integrated EDX. Electrons from the gun pass through LEEM optics and reflect off the sample to form an image on the detector. The orange region highlights the section of the system where EDX is performed, where an angled EDX detector detects X-rays generated by electron-sample interactions. Image sourced from [25]*

Electron Gun

Figure 2.2 shows a schematic of a field emission gun (FEG), which emits the electrons for the electron beam. They are pulled from a pointed single-crystal tungsten cathode, with a tip radius of curvature on the order of hundreds of nanometers. A strong electrostatic field, called the extractor voltage, is applied to the tip, lowering the surface potential barrier and allowing electrons to tunnel through and be emitted. These electrons are then accelerated to the desired energy, typically 10 or 15 keV, by an accelerator anode [13]. After acceleration, the beam passes through a magnetic gun lens, followed by a magnetic condenser lens, which together control the magnification and focus of the beam before it passes through the mag-

netic prism array.

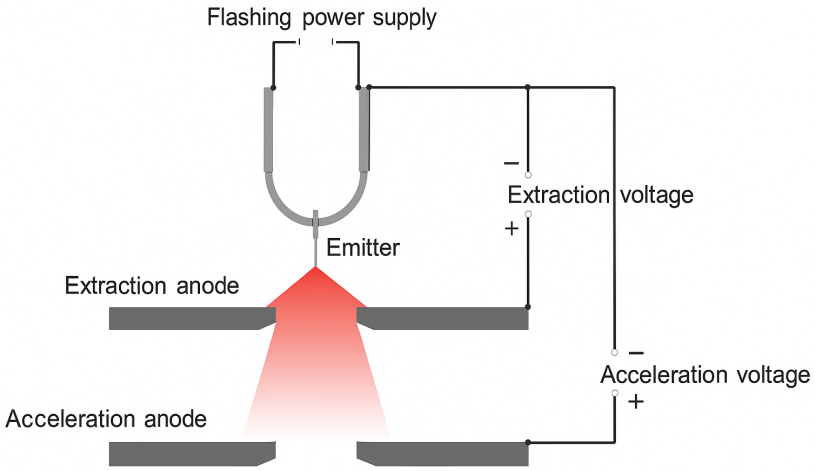

Figure 2.2: *Schematic of a cold field emission gun. Image sourced from [13]*

Prism array

After leaving the gun assembly, the electron beam passes through the first of two magnetic prism arrays. Each array deflects the beam by 90 degrees using five magnetic field segments, which guide the electrons along a curved path while maintaining astigmatic focus [25]. The first prism directs the beam toward the sample chamber, where the electrons interact with the sample and return to the prism to be deflected another 90 degrees further into the system. The second prism functions analogously: the beam enters from above, is deflected toward the electron mirror, and then to the electron detector.

Objective Lens and Sample Stage

After being redirected by the prism array, the electron beam enters the sample chamber through a transfer lens, which refocuses the beam into the back focal plane of the objective lens, and the objective lens then focuses the beam onto the sample surface. In addition to its optical function, the space between the sample holder and the objective lens contains an electric potential slightly lower in energy than the electron energy (bias

voltage).

This potential difference reduces the electrons' landing energy, allowing them to reach the sample with a controlled energy in the range of a few to several tens of electronvolts. After interacting with the sample, the same electrostatic field accelerates the electrons back through the objective lens with approximately the same energy they had upon incidence.

Electron Mirror

After passing through the sample chamber, the electron beam is directed toward the electron mirror, a relatively recent innovation in LEEM systems. The electron mirror plays an important role in correcting spherical and chromatic aberrations introduced by the objective lens. It consists of a tunable electrostatic potential well that reflects the incoming electrons without any physical surface interaction. By carefully tuning the mirror potential, these aberrations can be compensated, significantly improving image resolution and contrast [25].

Image Detection System

Finally, the image is projected onto a channel plate intensifier, which amplifies the electron signal. This is followed by a phosphor screen that converts the electrons into light, and the resulting photon image is captured by a CCD camera. The brightness and contrast of the resulting image can reflect many properties of a sample, such as surface morphology, crystallographic properties, electronic structure, and work function variations.

While LEEM provides high-resolution, surface-sensitive imaging of samples, in this project, its main role is to provide the electron beam and environment for EDX measurements. The focus is on quantitative chemical analysis, for which the LEEM has been equipped with an EDX setup. The following section will discuss the principles of EDX and its implementation into the ESCHER LEEM.

2.2 Energy Dispersive X-ray Spectroscopy

Energy Dispersive X-ray Spectroscopy (EDX) relies on the interaction between the primary electron beam and the sample material. These electrons can trigger various processes, one of which is the emission of characteristic X-rays unique to the elements present. This section takes a closer look at the physical principles behind EDX, setting the stage for how these signals are detected and how they can be used for quantitative analysis and interpretation of EDX spectra. To understand how these characteristic X-rays are produced, we first need to look at the different ways electrons interact with matter.

2.2.1 Electron-Sample interactions

Primary beam electrons interact with atoms of a sample in different ways, without interaction, with elastic interactions, or through inelastic interactions. The electrons penetrate the sample to a certain depth, and the volume within the sample where most interactions occur is known as the interaction volume. This region has a teardrop shape, which depends on both the energy of the incident electrons and the density of the sample material. As electrons travel deeper into the interaction volume, they lose more energy through successive interactions. This results in lower-energy processes occurring at greater depths within the sample. Below is a summary of the main interaction mechanisms:

Auger electron emission: In the top few nanometers of a sample, a primary electron can eject a core electron, and the resulting vacancy is filled by an outer-shell electron. The excess energy from this transition is transferred to another electron, which is then emitted from the atom. This process is highly surface-sensitive and forms the basis of Auger electron spectroscopy, a more surface-sensitive technique to perform compositional analysis of a sample.

Secondary electron emission: Secondary electrons (SE's) are emitted from the sample surface as a result of inelastic scattering. They originate from loosely bound electrons in the outer atomic shells that are ejected by energy transfer from primary electrons, electrons emitted from the source. Due to their low energy and limited escape depth, they are highly surface-sensitive and particularly useful for topographic imaging.

Version of August 27, 2025– Created August 27, 2025 - 11:10

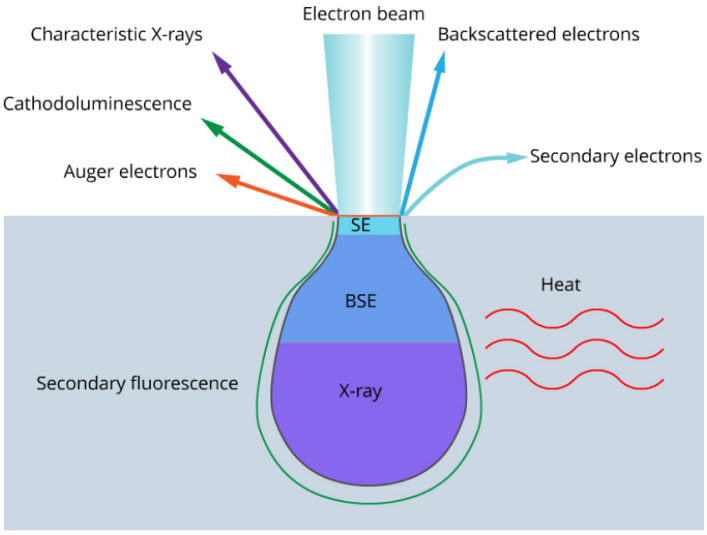

Figure 2.3: *Schematic of the interaction between the primary electron beam and the sample surface. Image sourced from [6]*

Elastic scattering: The first category of electron-sample interactions is elastic scattering, where atomic nuclei deflect electrons without significant energy loss. Many of these electrons are scattered back out of the sample, these backscattered electrons (BSE's) are useful for imaging and provide information about the sample's composition and topography.

Cathodoluminescence: In certain materials, inelastic scattering of primary electrons can excite electrons across the band gap. As these excited electrons relax back to lower energy states, they can emit photons. This process is known as cathodoluminescence. A well-known example is the light emitted by the phosphor-coated inner surface of a cathode ray tube (CRT) when struck by an electron beam. This emission is characteristic of the electronic and optical properties of a material, forming the basis for cathodoluminescence microscopy and spectroscopy, which are used to study properties such as band structure, defects, and crystal structure.

Phonon excitation (heating): Primary beam electrons can also induce lattice vibrations (phonons) in a sample, causing the sample to heat up. This effect forms the basis for electron energy-loss spectroscopy (EELS), an analytical technique which can provide information about the sample's composition, chemical state, electronic structure, and even thickness [27].

2.2.2 X-ray Generation Mechanisms

The final interaction mechanism we will discuss is the emission of X-rays, which plays the central role in EDX. X-rays are generated in the deeper section of the interaction volume and result from a more energetic process than cathodoluminescence. X-ray emission happens in two forms: characteristic X-rays and Bremsstrahlung emission, both will be discussed below.

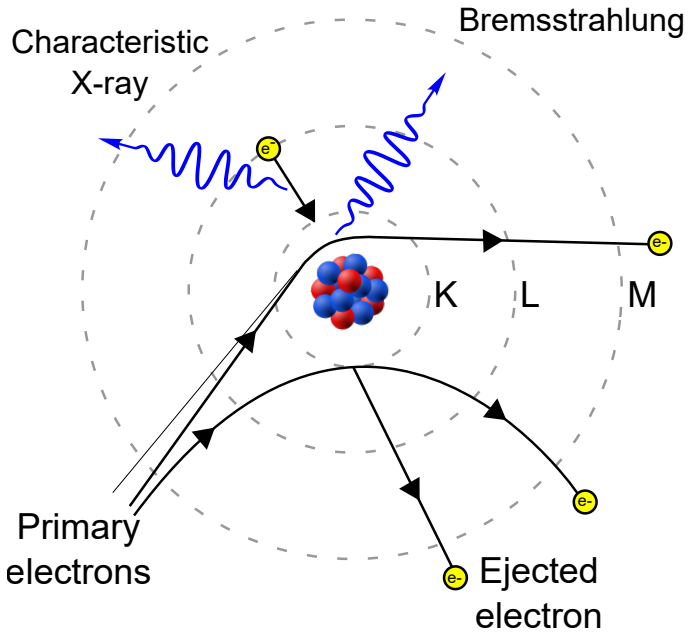

Figure 2.4: *Schematic of X-ray generation mechanisms. A primary electron ejects a K-shell electron, after which an L-shell electron fills the vacancy, emitting a characteristic X-ray. Another primary electron is deflected by the nucleus, emitting Bremsstrahlung radiation due to its deceleration in the Coulomb field (own work).*

Characteristic X-ray radiation

Characteristic X-rays are emitted when a primary electron ejects a core-shell electron, creating a vacancy in the atom. This vacancy is then filled by an electron from a higher energy shell, and the difference in binding energy is released. This excess energy can either be transferred to another electron, resulting in Auger electron emission, or be emitted as an X-ray photon. In the latter case, the X-ray photon has an energy equal to the difference in binding energies between the two shells, producing a sharp spectral peak that is characteristic of specific electronic transitions.

Version of August 27, 2025– Created August 27, 2025 - 11:10

Characteristic X-rays are named according to the shell where the initial vacancy was created, such as K, L, or M. This is followed by a Greek letter that indicates the shell from which the electron transitioned: α corresponds to a transition from the next outer shell, β from the one beyond that, and so on. If the originating shell contains subshells due to spin-orbit splitting, numbers are added to distinguish between the resulting spectral lines. For example, if a vacancy is created in the K shell and it is filled by an electron from the L_2 subshell, the line created by the transition is labeled $K\alpha_2$. Each characteristic X-ray line has a specific energy that is unique to each element. This forms the basis of how EDX can distinguish between elements in a sample. An overview of common X-ray transitions and their corresponding nomenclature is shown in Figure 2.5.

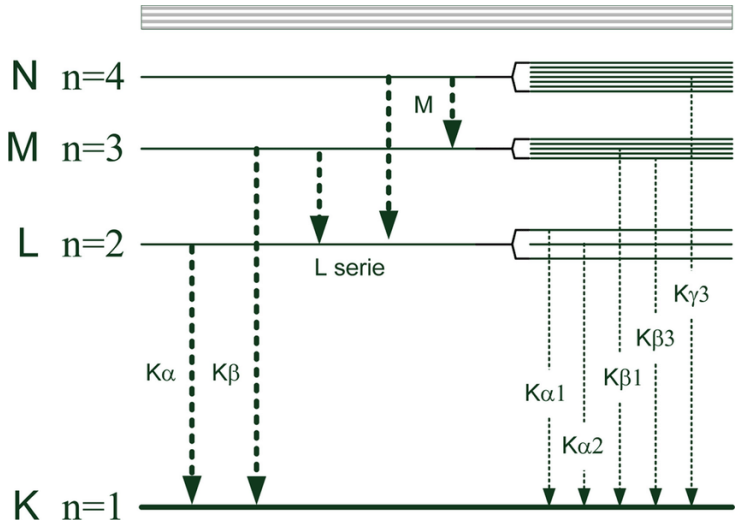

Figure 2.5: *Nomenclature of X-ray lines. Image sourced from [7]*

As we increase in atomic number of atoms, more electron transitions become possible, resulting in a greater number of characteristic X-ray lines. Hydrogen and helium do not emit characteristic lines. From $Z = 10$, K-lines begin to split into K_α and K_β, from $Z = 20$ the L-lines become detectable, and above $Z = 40$ the first M-lines appear. However, not all characteristic lines are important or resolved in EDX analysis. For example, K_{α_1} and K_{α_2} are often so close in energy that they appear as a single peak in an EDX spectrum [7]. For the Cs_3Sb photocathode studied in this project, the analysis focuses on detecting the characteristic Cs L and Sb L lines as indicators of stoichiometry.

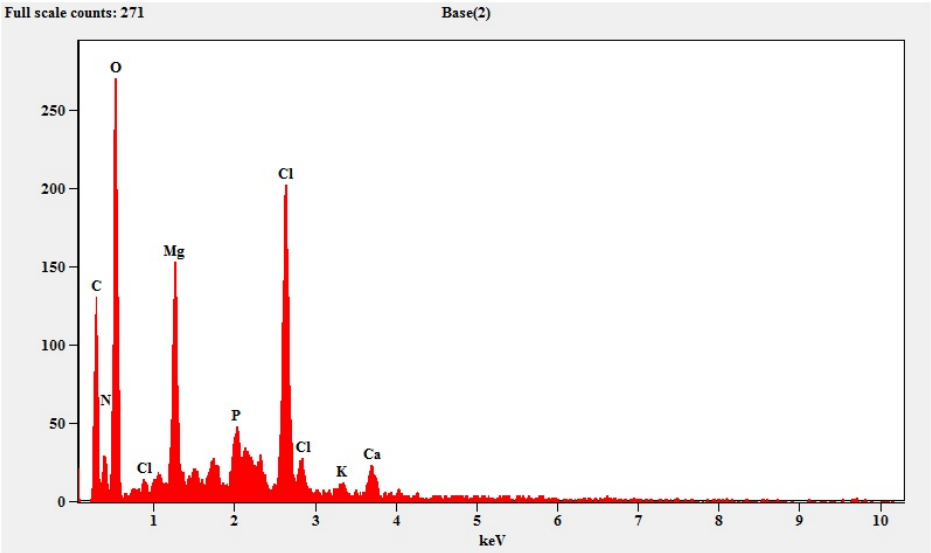

Figure 2.6: *An example of an EDX measurement showing characteristic line intensities and energies and their corresponding elements. Image sourced from [2]*

Bremsstrahlung radiation

Bremsstrahlung, directly translated from the German word for "braking radiation", is generated when a primary electron is deflected by the Coulomb field of an atom's nucleus. This deflection causes the electron to lose some kinetic energy, which is emitted as a photon. Unlike characteristic X-rays, which have discrete energies related to specific electron transitions, Bremsstrahlung is emitted in a continuous spectrum of energies. The spectrum has a range of energies from ~ 0 up to E_0, the energy of the primary electrons. Since the photons cannot have more energy than the incident electrons, this limit is called the *Duane-Hunt Limit* [6].

The spectral distribution of the intensity of Bremsstrahlung produced by an atom is given by Kramer's Law, derived by Hendrik Kramers in 1925 [4].

$$I(E) \approx \frac{IZ(E_0 - E)}{E}$$

With I the electron beam current, Z the average atomic number, and E_0 the primary beam energy. The intensity is inversely proportional to the X-ray energy, which correlates to lower energy deflections being more probable. However, Kramers' law does not account for the absorption of X-rays within the sample, which is significant at low energies and reduces

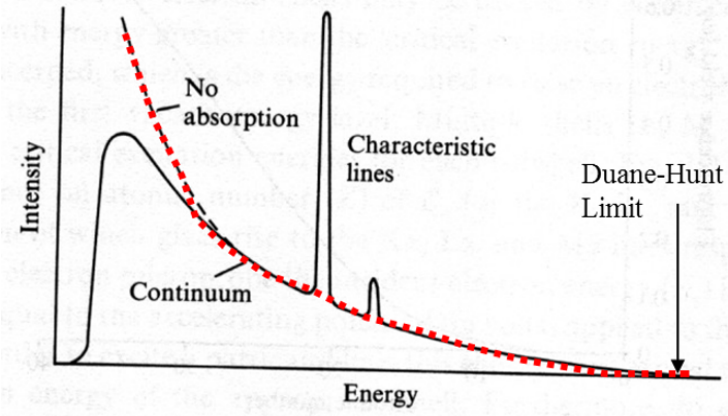

Figure 2.7: *Hendrik Kramers described the distribution of X-rays produced when electron beams hit a solid target, thus producing the continuum or bremsstrahlung radiation. As you can see from the red line (bottom right), ideally, the intensity of low-energy range X-rays should be very high, but in practice, we observe this not to be the case, due to absorption effects. [20]*

the measured intensity, resulting in a Bremsstrahlung spectrum that rises from zero, peaks at an energy roughly at a third of the incident energy, and then decreases toward the Duane-Hunt limit. The full spectrum, consisting of the characteristic X-ray radiation and the bremsstrahlung, is shown in Figure 3.5

2.2.3 X-ray Detection

An EDX detector is used to convert the energy of incoming X-rays into a digital signal. The detector has the following components:

- A collimator to ensure the measurement area is on the sample.
- An electron trap to collect scattered electrons, which would otherwise hit the detector, consists of two electrodes with a potential to pull electrons to the cathode.
- A window to isolate the detector.
- A silicon-drift-detector (SDD)
- A field-effect transistor (FET)
- A Multi-channel-analyzer.

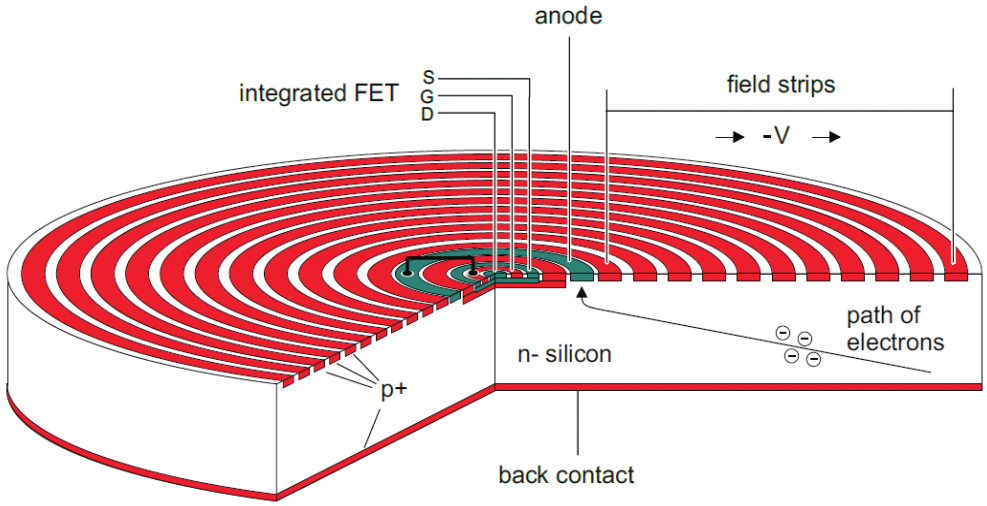

Figure 2.8: *Schematic layout of a cylindrical Silicon Drift Detector. The dotted line represents the diagonal shape of the drift field inside the bulk. Image sourced from [22].*

Silicon Drift Detector

The SDD is the core component in our EDX setup, operating by converting incoming X-ray photons into charge pulses. The silicon drift detector (SDD) consists of a fully depleted, high-resistivity silicon wafer with concentric drift rings that create a radial electric field guiding electrons toward a small central anode. It often includes an integrated field-effect transistor (FET) for low-noise signal amplification. When an X-ray photon enters the silicon crystal, it is absorbed and its energy generates electron-hole pairs in the semiconductor. The number of pairs produced is directly proportional to the energy of the incoming X-ray, approximately 3.8 eV per pair in silicon [7]. For example, a Ni Kα photon of 7.477 keV produces around 1968 pairs, while an Al Kα photon of 1.487 keV yields about 391 pairs. A high bias voltage across the crystal drives the electrons and holes toward opposing electrodes. The electrons drift toward the central anode from the large-area front contact through the radial electric field.

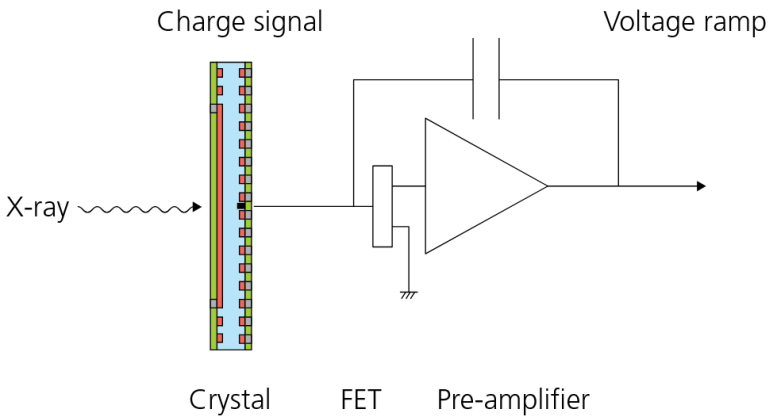

Figure 2.9: *Schematic of SDD connected to FET preamplifier and feedback capacitor. Image sourced from [12]*

FET

Attached to the anode is a field-effect transistor (FET), which acts as a charge-sensitive preamplifier, converting. The collected charge is deposited on a small capacitor at the FET input, inducing a voltage step according to $V = Q/C$ over the transistor. The resulting pulse, with amplitude proportional to the X-ray energy, is then passed to the pulse processor and multichannel analyzer (MCA) for digitization and spectral analysis.

Pulse Processor

After an X-ray photon is absorbed in the detector, the resulting charge pulse is amplified and shaped into a voltage signal. This shaping is characterized by the peaking time, also known as the processing time, the duration the pulse processor takes to average over the voltage signal after a count has been registered. Short peaking times allow high count rates but may compromise energy resolution due to increased noise. In contrast, longer peaking times yield cleaner, better-resolved pulses, but lower the count rate, as additional counts cannot be registered during this time.

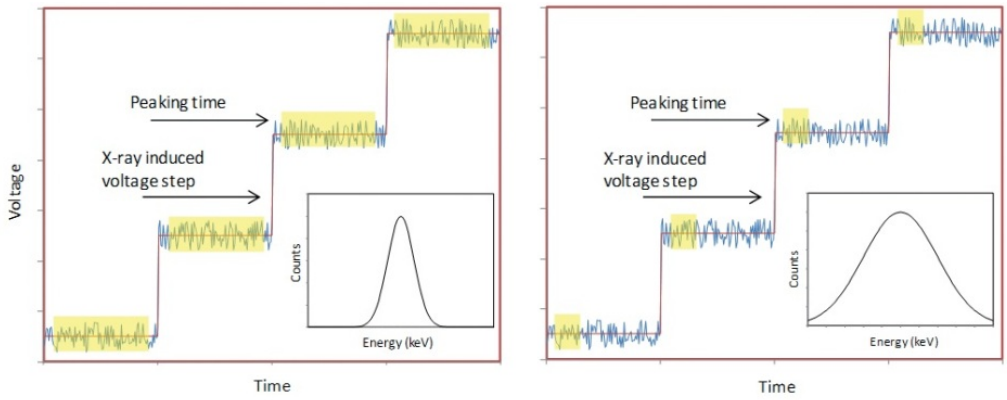

Figure 2.10: *Illustration of voltage steps as a function of an absorbed X-ray. The noise fluctuations demonstrate the impact of noise and shaping time (left vs right) on resolution. Image sourced from [24]*

This trade-off introduces the concept of dead time, the percentage of total acquisition time during which the detector is busy processing and cannot accept new events. Dead time increases with higher count rates or longer peaking times and can lead to significant undercounting if left uncorrected. Modern pulse processors continuously monitor and report dead time as a percentage of total measurement time. For reliable quantitative analysis, the dead time is typically maintained between 40-60%.

The dead time can be estimated using the following formula:

$$\text{Dead time} = \left(1 - \frac{\text{OCR}}{\text{ICR}}\right) \times 100\%$$

Where *OCR* is the output count rate (processed X-rays per second), and *ICR* is the input count rate (X-rays hitting the detector per second).

MCA

After shaping, pulses are digitized by an analog-to-digital converter and sorted by pulse height into energy bins in the multichannel analyzer (MCA). Because the pulses are processed and digitized, the energy assigned to each bin is relative and must be calibrated afterwards. The MCA compiles a histogram of counts versus energy, which forms the EDX spectrum displayed by the MCA software.

2.2.4 Spectral features and artifacts

EDX spectra not only contain characteristic X-rays and Bremsstrahlung background, but also contain other features and distortions that can affect the spectra. These arise from alternative interactions within the sample and the detection system.

Fluorescence yield ω

The emission of Auger electrons and characteristic X-rays is a competing processes that occur when an inner-shell electron is ejected. The probability that the excess energy is released as an X-ray photon instead of being transferred to another electron is called the fluorescence yield, often denoted as ω. This yield depends strongly on the atomic number. Light elements (low Z) tend to release their excess energy through Auger emission, resulting in a low fluorescence yield, while heavier elements (high Z) more often emit characteristic X-rays. Intuitively, this is because in heavier atoms, the energy gaps between shells are larger, making it less likely that the energy is efficiently transferred to another electron and more likely that it is released as an X-ray photon.

Escape Peaks and internal fluorescence

Escape peaks occur when an incoming X-ray photon ionizes a silicon atom within the detector material itself. This can lead to the emission of a secondary Si Kα X-ray (1.74 keV), which escapes the detector. As a result, the measured energy is reduced by 1.74 keV compared to the original photon, producing a secondary peak, known as the escape peak. Escape peaks occur more for higher energy characteristic peaks.

The X-rays emitted from the silicon can also be reabsorbed by the detector, which produces a small Si Kα peak in the spectrum, even if there is no Si present in the sample. However, improvements in design and construction of SDDs have minimized these artifacts to negligible levels and may only appear in older detectors [6].

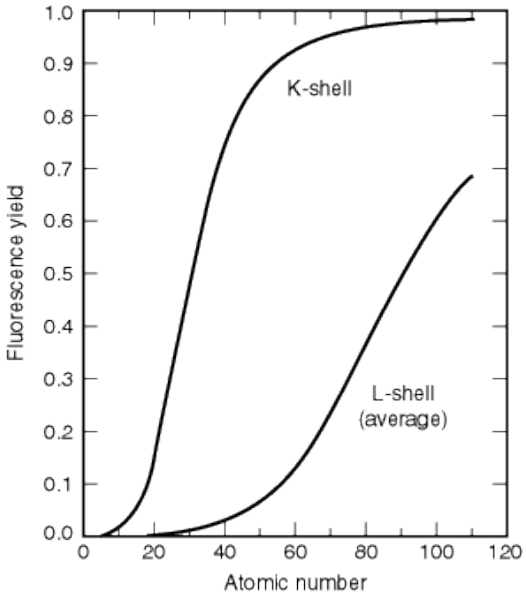

Figure 2.11: *Average fluorescence yields for K and L shells for Z between 5 and 110. The plotted curve for the L shell represents an average of L_1, L_2, and L_3 effective yields. Image sourced from [14]*

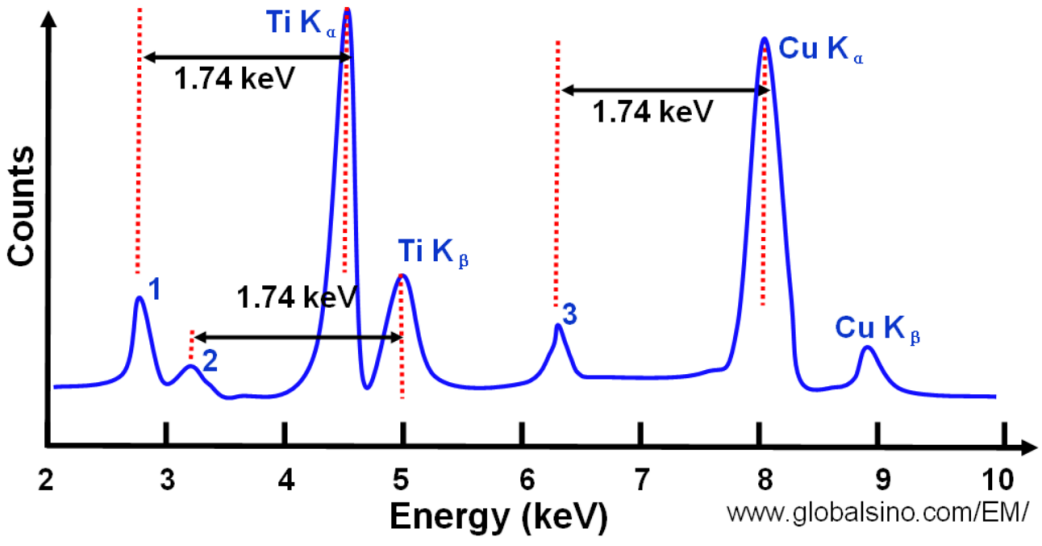

Figure 2.12: *Schematic illustration of the Si escape peaks for Ti Kα, Ti Kβ, and Cu Kα.Image sourced from [15]*

Sum Peaks

Sum peaks appear when two X-rays hit the detector in such a short time interval that the pulse processor cannot distinguish them. The processor then measures a single event with an energy equal to the sum of both X-rays. Sum peaks become especially visible at high count rates and shorter peaking times. Nowadays, spectrum analysis software can often recognize and account for both sum and escape peaks during processing.

incomplete charge collection

Incomplete charge collection (ICC) is a phenomenon in which not all electron-hole pairs created by an incoming X-ray are drifted to the electrodes, causing the measured energy to be slightly lower. In a sample, this typically occurs when X-rays are absorbed near the surface of the detector or in regions with imperfections, such as near grain boundaries, defects, or contamination layers. In these areas, electron-hole pairs can leak out, recombine, or get trapped before they reach the electrodes [12]. This leads to peak tailing on the low-energy side of characteristic lines, especially for low-energy X-rays that are absorbed closer to the detector surface.

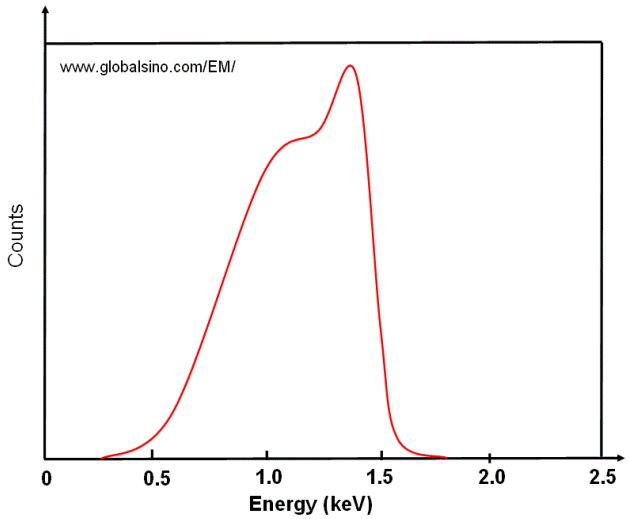

Figure 2.13: *Al Kα (1.486 keV) EDS profile obtained with an old Germanium detector. The noticeable shoulder on the low-energy side of the peak is produced by the incomplete charge collection. The relative magnitude of this shoulder depends on the energy of the peak. Image sourced from [15]*

This effect becomes more pronounced at low energies, where the X-rays do not penetrate deeply and charge collection is less efficient near the surface, causing the signal to be measured at a slightly lower energy. These events show up as a tail on the low-energy side of a peak. All detectors suffer from ICC to some extent. Low-energy X-rays have very shallow penetration depths and often interact near the front contact, where charge collection is less efficient. This makes low-energy peaks broader and lowers their apparent energy. In extreme cases, ICC can be the main factor limiting energy resolution at low energies.

Electronic Noise and Background

Electronic noise introduces background signals and limits the energy resolution of EDX detectors. One of the primary sources is voltage noise, which arises from thermal noise in all electronic components in the detector circuit. This noise can be reduced by averaging the signal over a longer period by for example increasing the peaking time in the pulse processor. In Figure 2.10, the effect of voltage noise is visible as fluctuations around the average.

A second contributor is leakage current through the detector, which is a form of shot noise. This leakage current is a result of the bias voltage applied in the sensor and shows as a slope in the voltage signal. Shot noise becomes significant at long peaking times, where the readout signal may drift upwards. The leakage current increases with both the sensor's area and thickness and is strongly temperature dependent. To minimize this effect and achieve optimal resolution, the detector is cooled using a Peltier stack connected to the system's water cooling, which cools the detector to approximately 230 K [19].

Both sources of electronic noise appear in the spectrum as counts at low energies (0-200 eV), effectively adding a large amount of noise and potentially obscuring low-energy signals. To minimize this noise, the peaking time can be increased, as it reduces the noise bandwidth and lowers the energy range these noise counts reach. However, this comes at the expense of a reduced maximum counting rate.

Detection and Resolution Limits

The resolution of an EDX system is defined as the full width at half maximum (FWHM) of a characteristic X-ray peak. Once a spectrum has been calibrated and an energy scale has been assigned, the FWHM can be measured in electronvolts (eV) to assess the system's energy resolution. For comparison between systems, the Mn Kα line at 5.9 keV is commonly used as a standard reference. The width of a peak is determined by detector performance and the ability to minimize noise sources.

The detection limit describes the lowest elemental concentration or thin-film thickness that can still be distinguished above the background signal. It depends on the signal-to-background ratio, the total number of counts, and the presence of overlapping peaks. In practice, detection limits are usually in the range of 1-0.1% mass of a sample, but they vary depending on the atomic number, X-ray yield, and detector sensitivity.

2.3 Quantitative Analysis in EDX

Quantifying an X-ray spectrum is the process of converting a measured spectrum into an estimate of the composition of the material it came from. In a way, this is quite straightforward: the spectrum from even a complex sample can be thought of as a sum of spectra from the individual elements that make it up. If the spectra of the individual elements are known, you can estimate what a mixture of those elements would look like. Regardless of the software or algorithm used, this is the basic idea behind all X-ray quantification. The result of such quantification is a composition, usually reported as mass fractions or as atomic fractions, which directly correlates to sample stoichiometry.

Quantitative EDX analysis methods can generally be divided into two categories: standardless and standard-based. The main challenge in both approaches is dealing with how the surrounding material influences the X-ray response of a sample, a phenomenon known as the matrix effects.
The sample matrix refers to the bulk material, this matrix affects both the generation and absorption of characteristic X-rays. For example, electron backscattering depends on atomic number, some emitted X-rays may be reabsorbed by the material, and secondary fluorescence can occur when X-rays excite nearby atoms. These combined effects, known as matrix effects,

must be corrected for to achieve meaningful and accurate compositional analysis.

2.3.1 Standardless Quantification

Standardless quantification estimates elemental concentrations by comparing measured X-ray intensities with theoretical sensitivity factors. These approaches often use tabulated data to approximate matrix effects through simplified corrections, such as ZAF or Phi-Rho-Z models.

While standardless methods can be useful for quick qualitative checks or simple, uniform samples, their accuracy is limited by assumptions about sample thickness, geometry, and composition, as well as by the specifics of the detector and measurement setup. In principle, a setup must be carefully quantified in the calculations for the standardless quantification to be reliable. This is especially difficult in our case, as the LEEM-EDX configuration used in this work is relatively new and non-standard. Because of these limitations, we opted for a standards-based approach instead.

2.3.2 Standard-Based Quantification

Standard-based quantification relies on comparing the X-ray spectrum of an unknown sample to that of calibration standards, which are spectra from pure samples with known compositions that have been measured under the same conditions. These standard spectra contain the known X-ray responses of specific elements and are used to match the peaks found in the unknown spectrum. To ensure accuracy, both the sample and standard must be measured under nearly identical conditions, including the same beam energy, detector geometry, and pulse processing settings.

In this approach, the intensity of each elemental peak in the sample is compared to the corresponding peak in the standard. This yields a ratio, commonly referred to as the k-ratio, which is then corrected for matrix effects using a correction model to determine the elemental composition. For this method to work, details such as the standard's composition, beam conditions, and measurement time must be well-documented and stored together with the reference spectrum. This strategy makes standard-based methods more reliable than standardless methods.

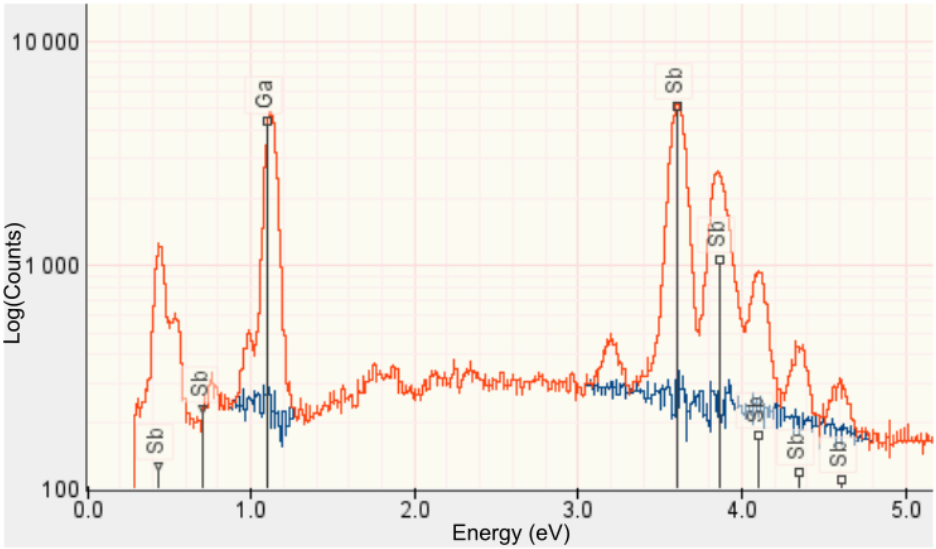

Figure 2.14: *EDX spectrum from a GaSb measurement, showing the fit and residual. Red: measured GaSb spectrum. Blue: residual after MLLSQ fitting.*

MLLSQ Fitting for Spectrum Decomposition

A key part of standard-based quantitative analysis is the accurate decomposition of measured spectra into contributions from individual elements. In this work, a Multiple Linear Least Squares (MLLSQ) fitting approach was used to express the unknown spectrum as a linear combination of standard spectra. This method determines the relative contributions of each element by minimizing the residual between the fitted model and the measured data.

The quality of the fit can be evaluated by examining the residual spectrum, which is what remains after the fitted signal has been subtracted from the measured spectrum. Ideally, a good fit removes all characteristic peaks, and the residual mainly shows the background. If characteristic peaks or sharp features remain in the residual, this indicates that the fitting model did not fully capture the measured spectrum, and the result may be unreliable. Figure 3.5 shows an example of such a fit on a GaSb measurement, where the residual is plotted alongside the original data.

Matrix Effect Correction Algorithm

The MLLSQ fits provide the relative intensities of each element's characteristic X-ray peaks, but these raw values are not directly proportional to the atomic composition because matrix effects must be corrected.

A simplified physical model, the extended Pouchou-Pichoir (XPP) algorithm [18], was used to estimate depth-dependent absorption and fluorescence effects and apply element-specific correction factors.

The following theoretical models and datasets were also used in the correction procedure:

- **NIST Standard Reference Database 126 (SuperSet 2005)** for mass absorption coefficients [21].
- **Acosta 2002** for Bremsstrahlung angular distribution modeling [3].
- **Bote and Salvat 2008** for ionization cross sections [8].

These corrections are applied to each fitted peak to obtain corrected intensities, which are then normalized and converted into atomic or mass fractions.

Monte Carlo Simulations

An alternative method for quantitative analysis is to compare the measured spectrum to Monte Carlo simulations, where electron trajectories and their interactions are statistically modeled to reproduce the X-ray spectrum of a sample with known composition and structure.

The simulation parameters must match the experimental setup, including beam energy, detector geometry, and sample composition. By adjusting parameters such as layer thickness or composition until the simulation matches the data, an estimate of the sample composition can be obtained.

Monte Carlo simulations are particularly useful for complex sample geometries such as thin films, multilayers, or non-planar shapes, where analytical models are inaccurate. However, they are more computationally demanding and less practical for large datasets.

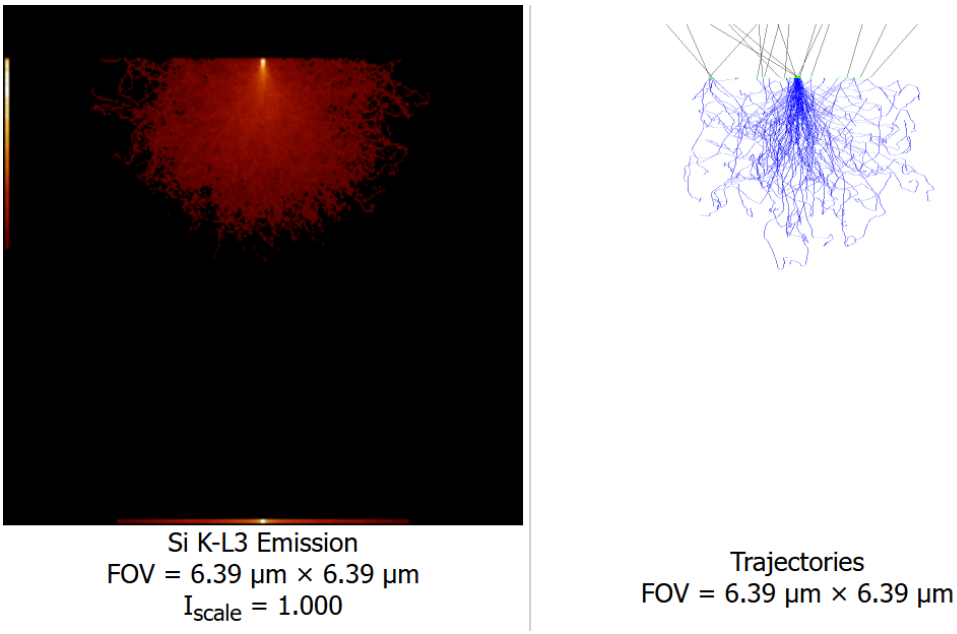

Figure 2.15: *Example Monte Carlo emission maps in DTSA-II. Left: simulated X-ray emission map for a Si substrate. Right: simulated electron trajectories showing beam penetration and scattering.*

2.3.3 Application to LEEM-EDX Measurements

MLLSQ fitting with XPP correction is designed for bulk samples and does not properly account for thin-film geometry. However, in this project, it was assumed that the signal from the thin film would still provide a reasonable estimate of stoichiometry. By comparing the characteristic peak ratios of Cs and Sb, the depth-related effects were considered to have a limited effect, especially given that most of the X-ray signal originates from the upper layers of the sample.

To better account for film geometry, we can perform Monte Carlo simulations on a thin film sample. One example is shown in Figure 2.15, which visualizes the X-ray emission profile from a 25 nm Cs_3Sb film on silicon. Such simulations offer a way to assess whether the bulk approximation used in the MLLSQ fitting still leads to valid compositional estimates for thin films.

Chapter 3

Experimental Methods

3.1 Experimental Setup

3.1.1 EDX Setup

EDX Detector

All EDX measurements were performed using an Amptek FAST SDD, a silicon drift detector that differs from traditional SSDs by incorporating a built-in CMOS preamplifier to reduce capacitance and electronic noise, resulting in improved energy resolution at short peaking times. The detector is mounted at a 20-degree takeoff angle inside the LEEM chamber. It features an active detector area of $17mm^2$, a detector thickness of 500μm, and is equipped with an Amptek C2 window consisting of silicon nitride (Si_3N_4) with an aluminum coating. Theoretically, the detector achieves an energy resolution of 122 eV FWHM at 5.9 keV and supports count rates exceeding 10^6 counts per second. However, such high count rates were not observed in this study, likely due to the X-ray fluorescence of the samples being relatively low in the setup.

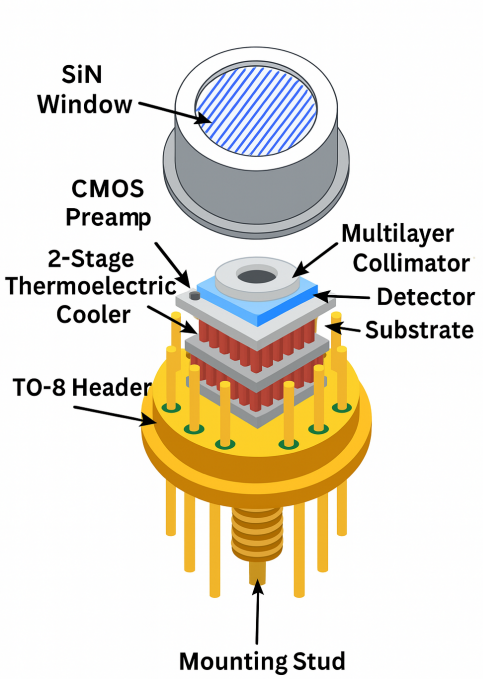

Figure 3.1: *Schematic illustration of the Amptek FAST SDD detector system. Image sourced from [1]*

EDX Column

The detector is mounted on a copper heat sink that passes through a vacuum flange, allowing both electrical connections and heat dissipation via the copper rod. The rod passes through an electron deflector set at -2.5 kV to attract stray electrons and prevent them from striking the detector. The EDX column includes a retractable bellow, allowing the detector assembly to be withdrawn when not in use. When retracted, a vacuum valve closes the connection between the EDX column and the main chamber, protecting the detector and maintaining the vacuum integrity of the main chamber.

The detector output is connected to an Amptek PX5 digital pulse processor, which performs signal shaping and pulse height analysis. The processed signals are then fed into a multichannel analyzer (MCA), which is connected via USB to a laboratory PC for data acquisition and storage.

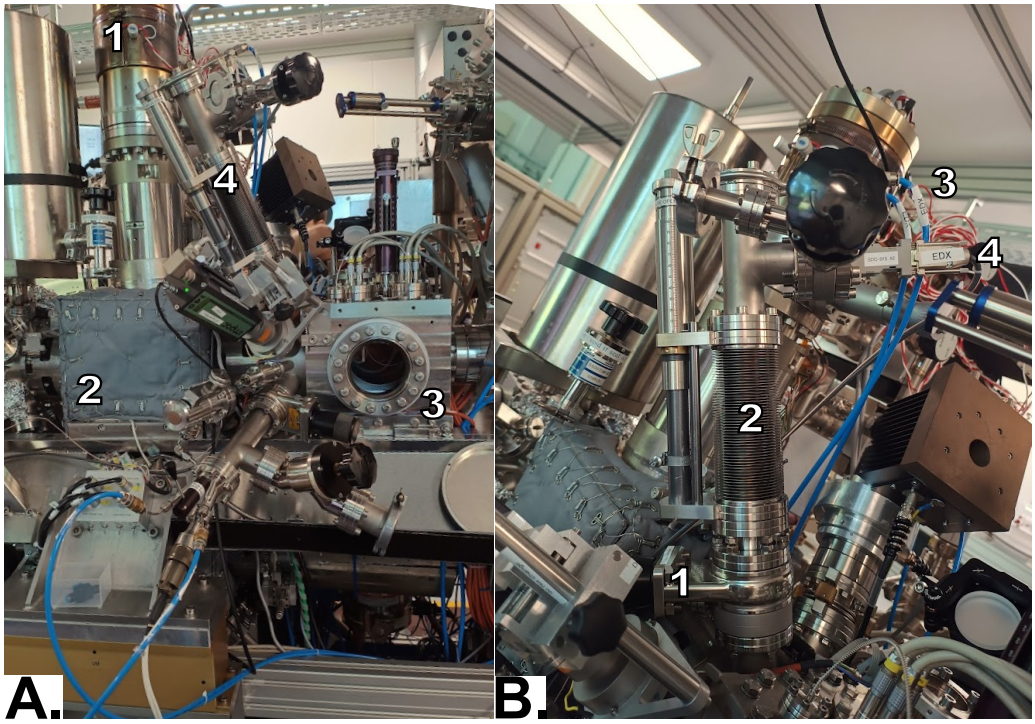

Figure 3.2: ***A.*** *Overview of the LEEM setup: 1. Electron gun; 2. First electron prism; 3. Main chamber housing the sample; 4. EDX column.* ***B.*** *Details of the EDX column: 1. Vacuum valve isolating the EDX column from the main chamber; 2. Retractable bellow; 3. Water cooling tubes; 4. Connection to the MCA*

3.1.2 LEEM Beam Settings and Geometry

The electrons come from a cold field emission gun, which uses a sharply pointed single-crystal tungsten tip to emit electrons by quantum tunneling under a strong electrostatic field. Although cold field emitters give a very bright and coherent beam, their emission current is inherently unstable. This instability happens because the electron emission depends heavily on the atomic-scale condition of the tip, like surface contaminants or small changes in vacuum, which can cause fluctuations in the current. In practice, this meant that the beam current often varied significantly between sessions. And unfortunately, during the project, the emission current had been very unstable due to contaminants and a degraded vacuum pressure. To reduce this instability, the gun was conditioned before each session by flashing the tip to remove contaminants and stabilize the emission current as much as possible.

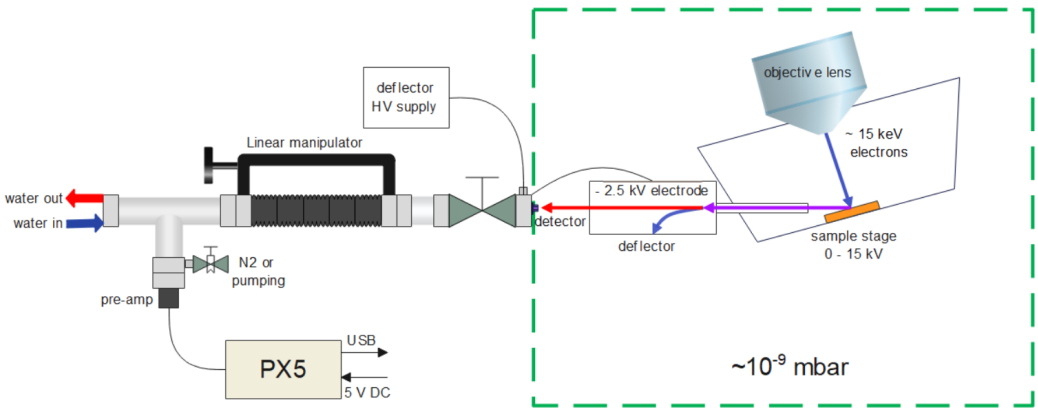

Figure 3.3: *Schematic of the EDX setup in the LEEM. Image sourced from [19]*

Because of this, cold field emitters are usually the least preferred electron sources for EDX experiments. Instead, thermionic or Schottky emitters are favored since they provide a more stable and consistent current, which results in steadier X-ray signals and better quantitative accuracy.

For all measurements here, the electron beam energy was set to 15 keV. This energy allows excitation of the main characteristic X-ray lines of interest and is the normal operating voltage for the LEEM. The EDX detector was fixed at a 20-degree takeoff angle from the sample surface.

Since the samples were fairly uniform, knowing the exact spot where the beam hit was not essential. The beam was roughly aligned using LEEM imaging, therefore, the sample bias was turned on. After that, the bias was switched off to let the beam hit the sample at 15 keV. Turning off the bias disabled imaging, so it was not possible to ensure a good beam position. Instead, the beam hitting the sample was confirmed through the EDX signal.

3.1.3 Pulse Processing and MCA Settings

All EDX spectra were acquired using the Amptek PX5 digital pulse processor. During the initial measurement sessions, a trial-and-error procedure was conducted to optimize the MCA and pulse processor settings. The main objectives were to achieve a stable and reliable dead time between 40 and 60%, balance count rate with spectral resolution, and minimize low-voltage noise.

The low-energy noise was suppressed by applying the "slow threshold" setting, which effectively sets the lowest channels of the spectrum to zero, as they will mainly contain noise counts. In our settings, the slow threshold was set to 1.953%, corresponding to the omission of approximately the first 40 channels. Given the energy calibration of approximately 7.4 eV per channel, this cutoff excludes signals below about 296 eV. This is considered a good low-energy cutoff, as the oxygen K_α peak, an important low-energy peak, occurs at 525 eV.

Table 3.1 summarizes the key MCA settings used during the majority of measurements. The peaking time was set to 1.600 μs to balance noise reduction with count rate, and the total gain was approximately 25. Detector temperature was maintained at 230 K to reduce leakage current and electronic noise.

Parameter	**Value**
Peaking Time	1.600 μs
Total Gain	24.996
MCA Channels	2048
Detector Temperature	230 K
Dead Time	40–60% (optimized)

Table 3.1: *Key MCA settings on the Amptek PX5 during EDX measurements.*

The final configuration represents a compromise between attaining good spectral resolution at short peaking times and handling the relatively low count rates typical for this experimental setup.

3.1.4 Software Tools

DPPMCA

The DPPMCA software was used during this project as the interface for the Amptek PX5 multichannel analyzer (MCA) on the lab computer. This program is supplied by Amptek and is required to operate the PX5 and detector, as it provides control over acquisition parameters and live monitoring of the detector output. It allows adjustment of acquisition settings, as well as real-time visualization of the spectrum during measurement.

However, the analysis capabilities of DPPMCA are limited to basic peak identification and simple intensity readout. As a result, the software was only used to set up and monitor the measurements. All data analysis was performed afterwards in DTSA-II.

DTSA-II

The main software used for creating standards, spectrum analysis, quantitative analysis, and Monte Carlo simulations in this project was DesktTop Spectrum Analyzer-II (DTSA-II), developed by Nicholas Ritchie at NIST [17]. It served as the primary workhorse for working with the measured spectra, including spectrum analysis, cross-referencing characteristic peaks, generating simulated spectra, spectrum fitting using MLLSQ, sample quantification, and calibrating spectrum files. DTSA-II is an open-source program for EDX measurements, combining user-friendly operation with modern algorithms to simulate, quantify, and plan energy-dispersive X-ray analysis. Its standard-based fitting and integrated correction models made it particularly suited for the challenges of EDX analysis in a LEEM system.

3.2 Calibration and Reference Standards

Quantitative EDX analysis relies on the use of calibration standards with known composition and well-defined stoichiometry. For the goals of this project, standards were required for both antimony and cesium. For accurate quantification, calibration standards should have a known quantity of your desired elements, be chemically stable, and be compatible with the LEEM setup.

3.2.1 Choice of Calibration Standards

Antimony: A suitable standard for antimony was readily available in the form of pure gallium antimonide (GaSb) wafers. These wafers have a well-defined 1:1 Ga:Sb stoichiometry. They were therefore ideal for use as a standard for the antimony. A piece of wafer was cut off and cleaned thoroughly using an acetone bath in an ultrasonicator, followed by an isopropyl alcohol bath. The sample produced a nice spectrum, which was usable as an EDX standard for antimony.

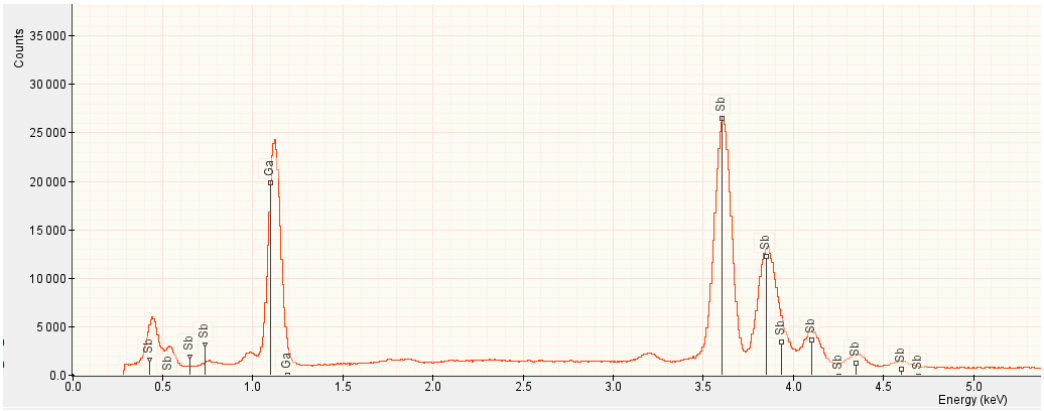

Figure 3.4: *The GaSb standard spectrum. measured for 18 minutes*

Cesium: Finding a reliable cesium standard was more difficult. Elemental cesium is a highly reactive alkali metal that combusts in contact with the atmosphere, and most cesium compounds have either an undefined stoichiometry or are unstable. However, cesium iodide (CsI) sputtering targets with a known 1:1 stoichiometry were available at the lab. Although CsI is hygroscopic and very soft, it was considered to be the most practical choice for use as a cesium standard.

Figure 3.5: *Picture of the polished CsI sample in a LEEM sample cap.*

The CsI sample required careful surface preparation. Due to its hygroscopic nature, the target surface would degrade upon exposure to air, due to it forming cesium hydroxide compounds over hours in normal humidity conditions [16]. To ensure a clean and uniform surface, the sample was polished using a fine 1800-grit sandpaper and cleaned with isopropyl alcohol immediately before insertion into the LEEM system. SEM images before and after polishing confirmed the removal of surface irregularities and reaction products.

(a) *CsI surface before polishing, showing roughness and contamination due to moisture exposure.*

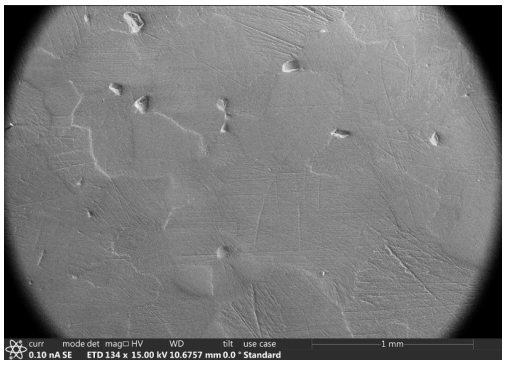

(b) *CsI surface after polishing with 1800-grit sandpaper, revealing a smoother and cleaner surface.*

Figure 3.6: *CsI surface after polishing, showing the surface contaminants have been successfully removed.*

Although CsI is an electrical insulator, no charging artifacts were observed during EDX measurements. This was further supported by the fact that the surface could be imaged in the SEM without excessive charging, suggesting that enough charge could disperse through the mount. Additionally, no spectral distortions indicating high-energy suppression were present.

The measurement produced a clear and usable signal for calibration as a cesium standard. However, it was not possible to quantify any oxygen from surface degradation, as the oxygen K_α peak overlaps with the M lines of both cesium and iodine at similar energies. This makes it difficult to separate the contributions from oxygen with confidence. As any remaining oxygen was expected to be minimal and the CsI signal remained well-defined, the oxygen contribution was omitted from the analysis, introducing some uncertainty in the cesium quantification but likely within the reported error margins.

3.2.2 Thin-Film Standards

Thin-film standards can be used for quantification in layered samples using models like the ζ-factor method, which account for depth-dependent X-ray generation. To explore this approach, a series of pure antimony films were deposited onto silicon substrates in the preparation chamber. These samples could, in principle, be used to calibrate thin-film EDX analysis. However, no suitable method was available to deposit a known-thickness cesium-containing layer with a defined stoichiometry. As a result, thin-film quantification based on matched reference layers was ultimately not pursued.

3.3 Measurement Procedure

The following procedure was used to perform EDX measurements in the LEEM system. It is presented step by step to allow future users to reproduce the setup and workflow.

1. **Prepare the EDX system:**
    - Open the vacuum valve between the main chamber and the EDX column.
    - Wait for the main chamber pressure to stabilize.
    - Turn on the water cooling system for the EDX detector.
    - Turn on the power supply for the electron deflector
    - Turn on the PX5 multi-channel analyzer.
    - Insert the Amptek FAST SDD detector in the chain chamber and power it on.
2. **Sample preparation and loading:**
    - Clean the sample.
    - Mount the cleaned sample in the LEEM sample holder and load it into the main chamber.
3. **Start the acquisition software:**
    - Launch the `DPPMCA` software on the acquisition computer.
    - Load the correct configuration file with optimized settings.

4. **Beam alignment:**
    - Use LEEM/PEEM imaging mode to roughly align the beam on the sample.
    - Once aligned, disable the sample bias to allow the beam to strike the sample at full energy (15 keV).
5. **Optimize detector signal:**
    - Switch to delta mode to verify that the detector is receiving a signal.
    - Slowly adjust the sample height (Z-direction) to maximize the signal.
    - Continue adjusting until the count rate stabilizes at its maximum value.
6. **Perform the measurement:**
    - Start the spectrum acquisition.
    - Allow the scan to run for the full preset acquisition time (typically 180 seconds).
    - After completion, save the data for further analysis.

3.4 System Characterisation Experiments

3.4.1 Electron Noise from Sample Bias

During early measurements, a strange noise feature was observed in the EDX spectra when the sample bias was active. It appeared as a broad hump at the high-energy side of the spectrum and shifted with increasing bias voltage. This noise was visible with the beam turned off. To investigate this, a series of measurements were performed at different bias voltages: 5, 7, 9, 11, 13, and 15 kV. For each setting, a spectrum was acquired for 5 minutes.

This noise was only present when the sample bias was enabled and disappeared entirely when the bias was turned off. The noise increased in intensity when the electron deflector was disabled and significantly reduced with the deflector enabled.

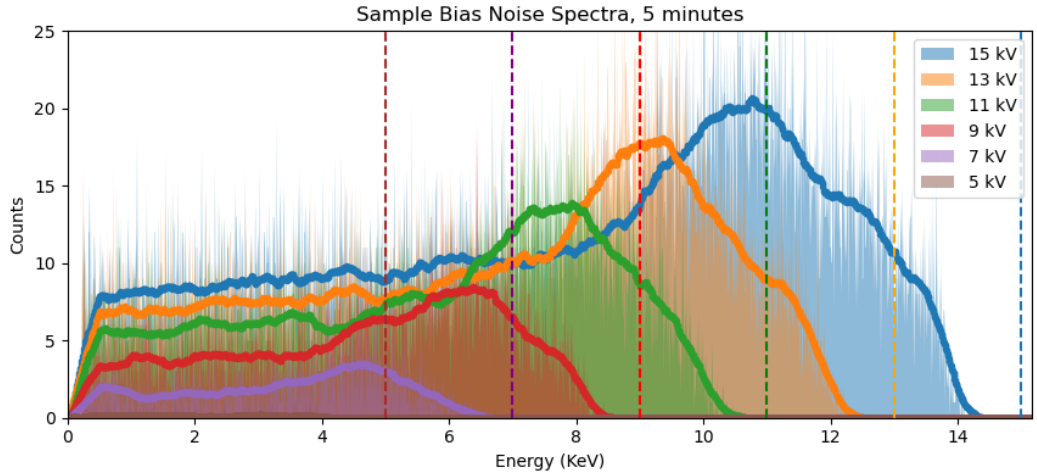

Figure 3.7: *Noise signal measured at different sample bias voltages with the electron deflector turned off. The hump-like feature shifts to higher energies as the bias increases.*

Despite being visible, the signal was weak, around 4 counts per channel per minute. The noise did not interfere with actual EDX measurements, but was not observed on its own before.

One possible explanation is that the signal originates from field emissions caused by the bias voltage. This sends high-energy electrons against the chamber's interior components, releasing X-rays which get picked up by the detector.

3.4.2 Sample-to-Lens Distance Optimization

A known issue was present with the EDX detector when the project was started, the EDX signal intensity was too low to be usable, often limited to a few hundred counts per second, which made meaningful analysis impossible. After several unsuccessful attempts, it was discovered that moving the sample stage approximately 1 mm on the Z-axis, which lies parallel between the objective lens and the sample, back from the standard LEEM measurement position significantly increased the signal. In some cases,s achieving count rates of up to 3-5 thousand counts per second.

The cause was determined to be a misalignment of the EDX detector column. At the default LEEM imaging Z-position of around 200 μm, the sample was misaligned with the EDX detector and partially blocked from the collimator's view. To characterize this effect, an experiment was performed where the sample Z-position was gradually varied and the count rate was recorded.

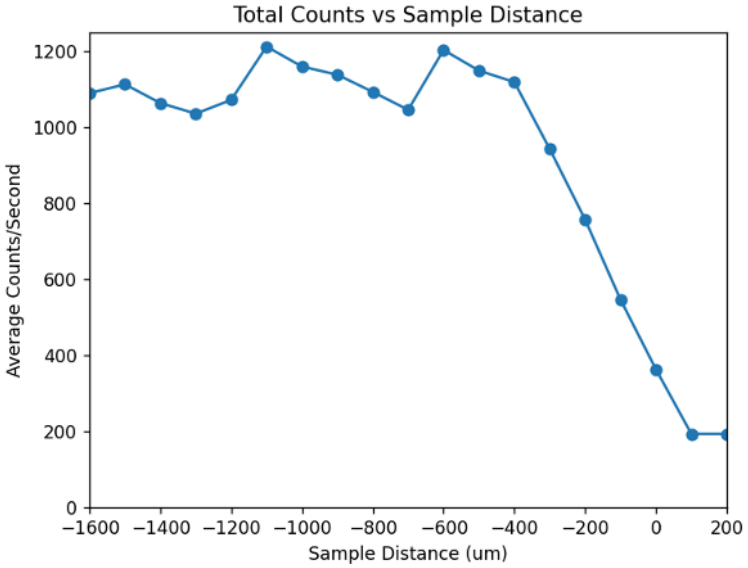

Figure 3.8: *EDX signal intensity as a function of the sample Z-position. The signal increases sharply after the LEEM focus position, peaking around 1100 cps before slowly declining.*

As shown in Figure 3.8, the signal improves significantly beyond the standard position. However, the optimal position varied slightly between sessions, likely due to changes in beam alignment. Therefore, before each measurement series, a quick sweep in the Z-direction was performed to find the position with the highest count rate.

Version of August 27, 2025– Created August 27, 2025 - 11:10

Chapter 4

Results

4.1 Cs_3Sb Samples

To evaluate the compositional analysis capabilities of the EDX system, three Cs_3Sb photocathode samples were prepared and measured under identical conditions. These samples varied in thickness and quantum efficiency (QE), but all were analyzed with the same EDX setup. The measurements were conducted in collaboration with Hugo Weisz BSc., who was optimizing photocathode QE. The goal was to gain insight into the stoichiometry of the photocathodes through EDX analysis.

4.1.1 Photocathode quantification using standards

The quantification was performed using the method described in section 2.3.2, and all measurements were taken under consistent conditions. It is important to note that the Si K Sum peak at 3.48keV lies very close to the antimony L_α peak at 3.604keV, which is the main peak used for fitting , complicating its clear identification. With the sum peak often being higher than the antimony peak .

First Sample

Date: 2 June 2024
Thickness: 15 nm **Quantum Efficiency (QE):** 3.75%
Measurement: Two measurements of 180 seconds each **Dead time:** $\sim$ 50%

The first photocathode, a 15 nm thin film representative of typical operational thickness, was measured to assess whether the LEEM-EDX system could resolve the expected stoichiometry at this scale. The EDX spectrum in Figure 4.1 shows minimal cesium and antimony signal, with only a faint cesium peak barely above the noise floor and no visible antimony signal. A slight shift of the Duane-Hunt limit to 14.65 keV suggests possible surface charging or beam misalignment. Quantification results in Table 4.1 show large uncertainties and an unrealistically high cesium-to-antimony ratio, confirming that at this thickness, the system struggles to detect antimony.

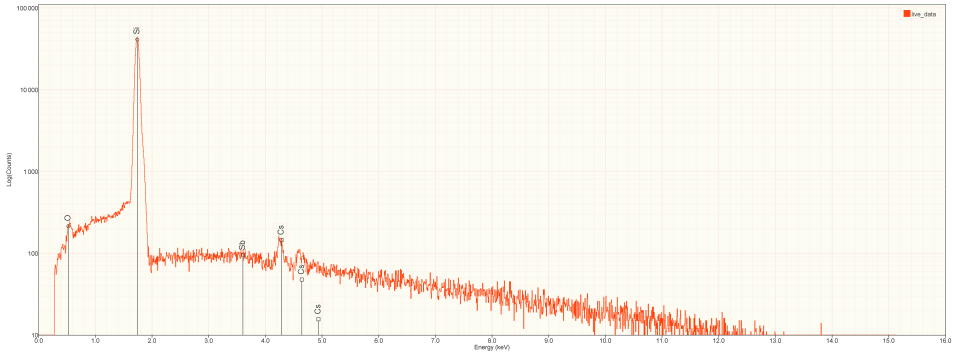

Figure 4.1: *Raw EDX spectrum of the first* Cs_3Sb *sample. The cesium peak is faint and barely above noise, while no antimony peaks are distinguishable.*

Element	Mass Fraction	Atomic Fraction	Atomic Ratio
Antimony	0.0032 ± 0.0031	0.1272 ± 0.1807	1
Cesium	0.0242 ± 0.0319	0.8728 ± 0.1807	6.86 ± 10

Table 4.1: *Quantitative EDX results for the first* Cs_3Sb *sample. Atomic ratio normalized to Sb = 1.*

The same sample was remeasured after eight days in vacuum to check for possible compositional changes over time. This time, with longer acquisi-

tion, the spectrum in Figure 4.2 showed a faint but now discernible antimony peak, though still partially obscured by the silicon sum peak. This improvement is likely due to changes in beam alignment rather than any change in the sample itself. Quantification in Table 4.2 still shows large uncertainties, with the weak antimony signal insufficient for a reliable fit.

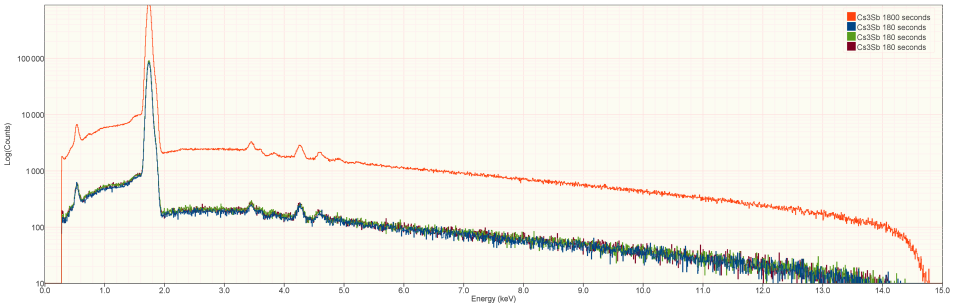

Figure 4.2: *EDX spectrum of the first sample remeasured after eight days.*

Element	Mass Fraction	Atomic Fraction	Atomic Ratio
Antimony	0.0022 ± 0.0026	0.1072 ± 0.1880	1
Cesium	0.0200 ± 0.0315	0.8928 ± 0.1880	8.33 ± 15

Table 4.2: *Quantitative EDX results for the first sample after eight days of vacuum exposure.*

Second Sample

Date: 10 June 2024
Thickness: 12 nm **Quantum Efficiency (QE):** 3.3%
Measurement: Three scans of 180 seconds each

The second sample, slightly thinner at 12 nm, produced results similar to the first. The EDX spectrum in Figure 4.3 shows a good cesium peak, but a very weak antimony signal, which is barely discernible and largely obscured by the silicon sum peak. Quantification (Table 4.3) gave an even higher cesium-to-antimony ratio, suggesting that the system remained near its detection limit for antimony at this threshold.

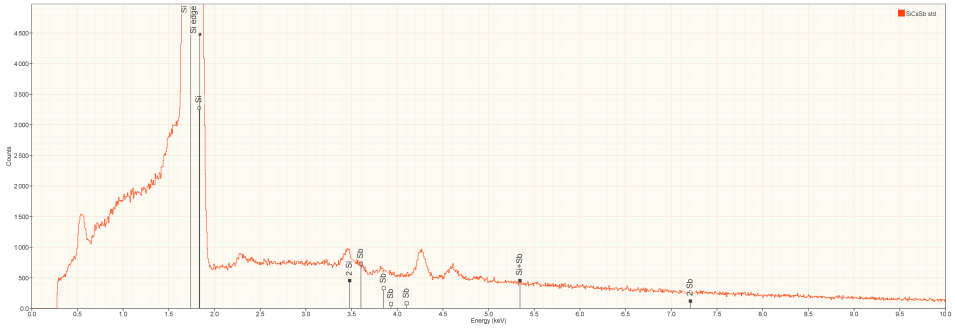

Figure 4.3: *EDX spectrum of the second sample, showing distinct cesium peaks and faint antimony signals.*

Element	Mass Fraction	Atomic Fraction	Atomic Ratio
Antimony	0.0012 ± 0.0015	0.0561 ± 0.1021	1
Cesium	0.0215 ± 0.0311	0.9439 ± 0.1021	16.8 ± 30

Table 4.3: *Quantitative EDX results for the second sample*

To check for possible compositional changes over a few hours, the sample was remeasured three hours later. The spectra before and after, shown in Figure 4.4, are nearly identical. While the overall intensity dropped slightly, likely due to beam instability or surface contamination, no significant changes in cesium or oxygen peaks were detected, and the already weak antimony signal remained obscured. Quantification (Table 4.4) confirms that no measurable degradation occurred in this timeframe, suggesting any QE loss observed may have occurred immediately after transfer to the main chamber.

Element	Mass Fraction	Atomic Fraction	Atomic Ratio
Antimony	0.0008 ± 0.0013	0.0479 ± 0.1168	1
Cesium	0.0164 ± 0.0312	0.9521 ± 0.1168	19.8 ± 50

Table 4.4: *Quantitative EDX results for the second sample, three hours after initial measurement*

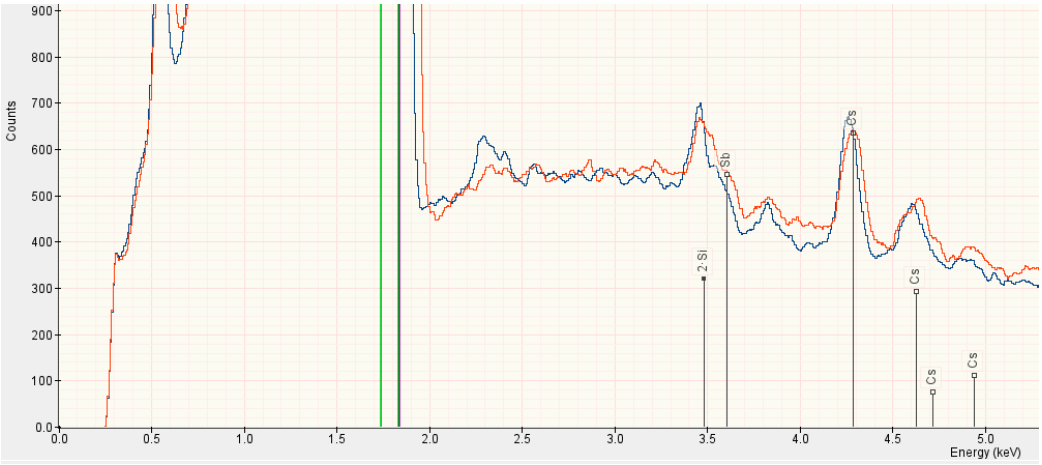

Figure 4.4: *EDX spectra of the second sample immediately after growth (blue) and three hours later (red). Both spectra are sums of three 180-second scans, smoothed for clarity.*

Third Sample

Date: 16 June 2024
Thickness: 25 nm **Quantum Efficiency (QE):** 2.3%
Measurement: Single measurement of 1800 seconds

The third sample, with a much greater thickness of 25 nm, finally yielded a clear antimony signal rising above the silicon sum peak. As shown in Figure 4.6, both cesium and antimony peaks are distinct, and quantification in Table 4.5 produced a ratio much closer to the expected stoichiometry. This suggests that the thicker film provided sufficient antimony to overcome the detection limit of the system. However, some interference from the silicon sum peak remains, as illustrated in Figures 4.6 and 4.7. Therefore, we might argue that the antimony content is still not sufficient.

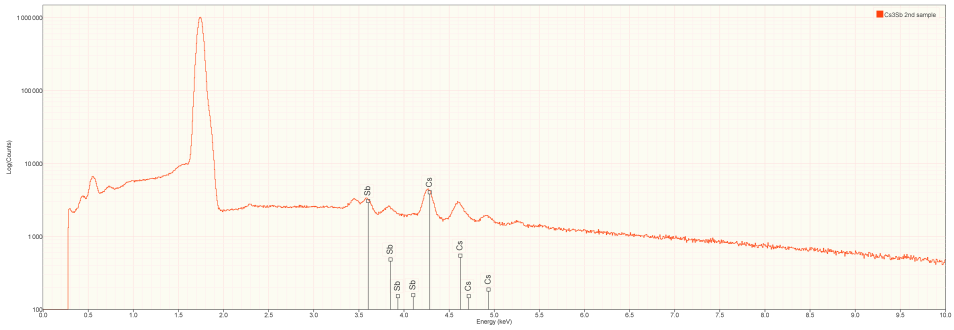

Figure 4.5: *EDX spectrum of the third sample showing distinct Cs and Sb peaks.*

Element	Mass Fraction	Atomic Fraction	Atomic Ratio
Antimony	0.0121 ± 0.0038	0.1695 ± 0.0835	1
Cesium	0.0649 ± 0.0326	0.8305 ± 0.0835	4.43 ± 3

Table 4.5: *Quantitative EDX results of the third sample.*

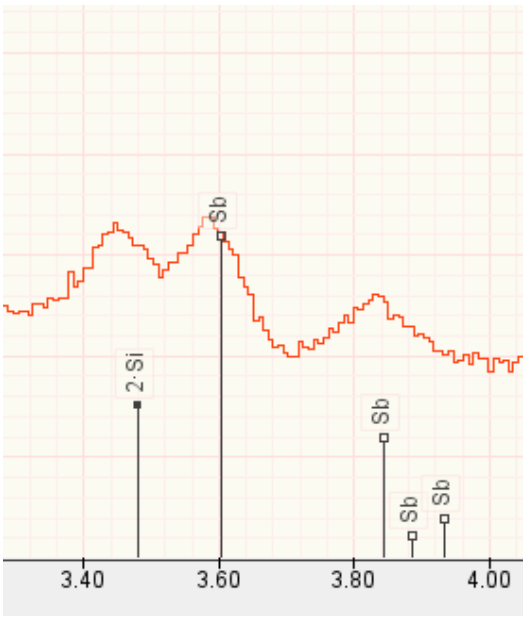

Figure 4.6: *Identified Si KαK sum peak adjacent to the Sb Lα peak.*

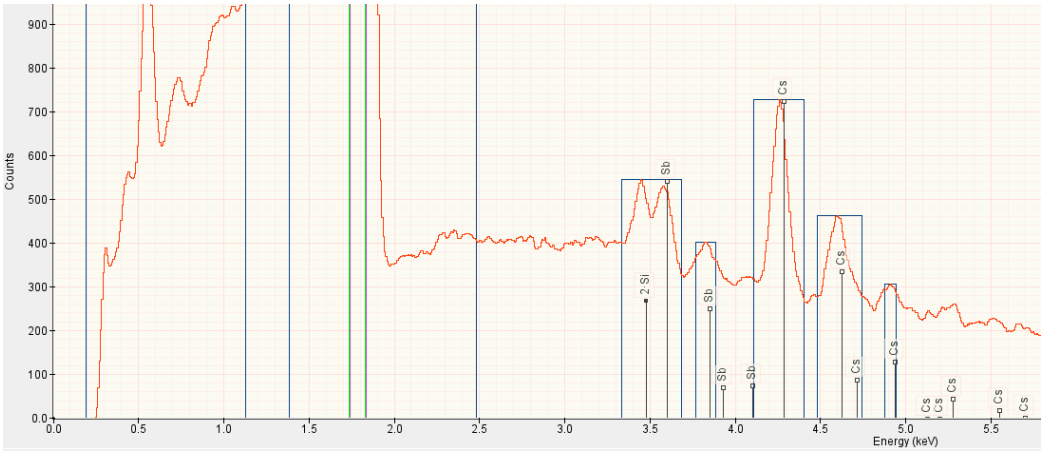

Figure 4.7: *Red: Sample spectrum; Blue: identified peaks.*

4.1.2 Monte-Carlo Simulation-Based Stoichiometry Estimation

Simulations were performed as mentioned in section 2.3.3 to evaluate the spectra expected from the photocathode. To account for variations in electron dose between experimental measurements, the electron dose parameter in the simulation was manually adjusted until the maximum of the silicon K_α peak matched that of the measured spectrum. Following this alignment, background subtraction was performed using the Clayton algorithm, and the relative peak intensities of cesium and antimony were compared between the simulation and the measurement.

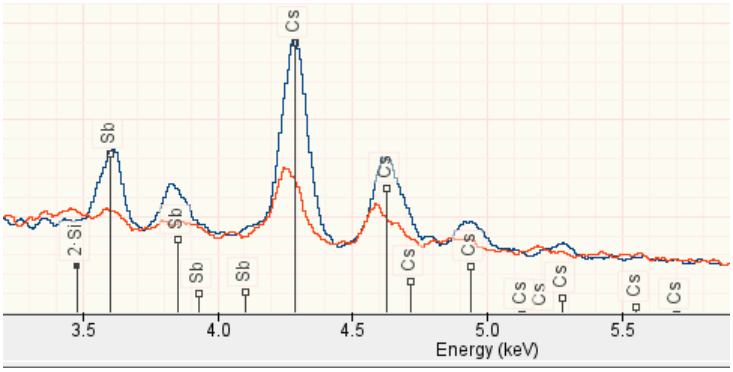

Figure 4.8: *Blue: Simulated spectrum, Red: real spectrum. Simulated vs experimental spectrum for Sample 1 (15 nm film).*

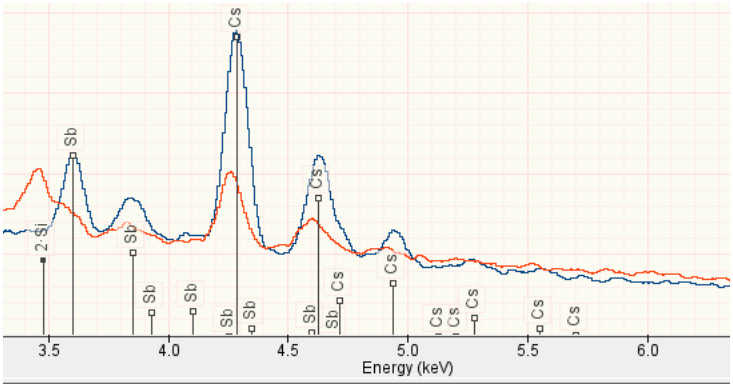

Figure 4.9: *Blue: Simulated spectrum, Red: real spectrum. Simulated vs experimental spectrum for Sample 2 (12 nm film).*

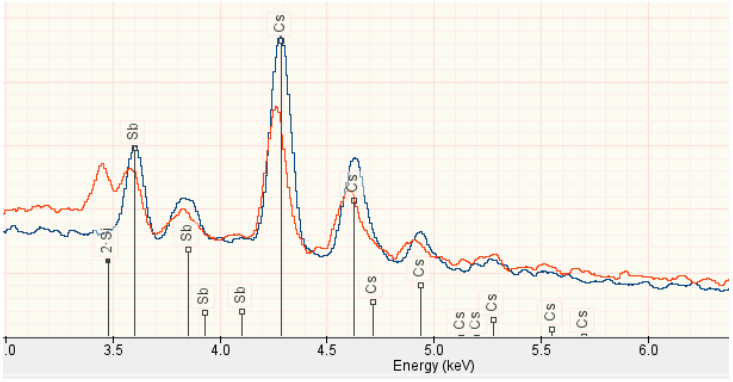

Figure 4.10: *Blue: Simulated spectrum, Red: real spectrum. Simulated vs experimental spectrum for Sample 3 (25 nm film).*

The simulated and measured spectra show several notable differences. The silicon background and K_α peak were matched successfully in all cases, confirming that the simulated dose was scaled correctly. However, the absolute intensities of the Cs and Sb peaks in the measured spectra were lower than those predicted by the simulation for each sample when compared to their respective Si K_α peak.

Several factors could account for this discrepancy. Surface oxidation or contamination may have reduced the effective X-ray yields for Sb and Cs. Uncertainty in the results may also be caused by inconsistent electron beam focus or illumination across the samples, as minor shifts in alignment could significantly affect the fluorescence of the sample.

To assess the stoichiometry of the samples more directly, each measured spectrum and its corresponding simulation were processed by removing the background using the Clayton algorithm and applying a smoothing filter. The ratios between the Cs L_α and Sb L_α peak intensities were then determined from these processed spectra and compared to evaluate how closely the measured compositions approached the expected stoichiometry.
The first sample exhibited a visible cesium peak, but no discernible Sb peak, despite both being present in the simulated spectrum. This may be due to beam misalignment, or the beam may have been focused on a region with an abnormal distribution of cesium and antimony.

In the second sample, the simulated Cs:Sb peak ratio was approximately 1:2.54, whereas the experimental result showed a ratio of 1:2.81, This is

most likely due to the fact that the Sb peak height could not be determined properly due to being obscured by the Si sum peak.

The third sample yielded the closest agreement between simulation and measurement, with a simulated Sb:Cs peak ratio of 1:2.33 and a measured value of 1:2.36. This close correspondence suggests that the sample's stoichiometry was near that of ideal Cs_3Sb. The quantitative MLLSQ fit also supported this conclusion, returning the most consistent compositional result of the three. However, it should be noted that this sample had the lowest quantum efficiency. The improved stoichiometric accuracy may therefore be attributed not to an optimal composition, but to the greater film thickness (25 nm), which produced a stronger EDX signal and improved the signal-to-noise ratio compared to the thinner samples.

Sample	**Simulated Ratio (Sb:Cs)**	**Measured Ratio (Sb:Cs)**
Sample 2	1:2.54	1:2.81
Sample 3	1:2.33	1:2.36

Table 4.6: *Comparison of Cs to Sb peak ratios in simulation and experiment.*

The DTSA-II simulations do not reproduce detector artifacts such as the silicon K_α sum peak near 3.5 keV, which complicates peak fitting the experimental data. This contributes to the challenge of accurately extracting the Sb signal from the measurements, especially for thinner samples with weaker signals.

Despite its limitations, the DTSA-II simulation approach still provided a useful way to evaluate the Cs:Sb stoichiometry. While it is less rigorous than the ζ-factor method, the results from Sample 3 showed good agreement between the simulated and measured spectra. This supports the trends seen in the MLLSQ fits and helps identify which samples came closest to the ideal Cs_3Sb ratio.

4.2 Antimony Thickness Series on SiN: Evaluation of Measurement Sensitivity

To assess the detection sensitivity and quantitative reliability of the EDX system for thin films, a series of pure antimony layers was deposited in 5 nm increments onto a SiN substrate. The five samples had thicknesses of 5, 10, 15, 20, and 25 nm. This experiment was meant to determine how the measured Sb signal scales with film thickness, and to what extent the film thickness influences the resulting EDX spectra in this setup.

Each measurement followed the same procedure: a layer of antimony was deposited and its thickness determined using a quartz crystal monitor (QCM). The sample was then transferred to the LEEM system, where two consecutive 180-second EDX scans were acquired and summed to improve signal integrity. Afterward, the sample was returned to the preparation chamber for the next deposition step. Throughout the series, all experimental parameters were kept constant, including the electron beam energy (15 keV), measurement geometry, and acquisition time. All spectra had similar dead times of approximately 50%.

Figure 4.11 shows the Sb L_α peak in the EDX spectra for each sample, with increasing Sb thickness from left to right. The Sb L_α peak at 3.604 keV increases steadily in height with each deposition step. At 5 nm, the Sb peak is barely resolved and lies well below the silicon sum peak. At 10 nm, the Sb signal surpasses the sum peak, and from 15 nm onward, it completely obscures it. These observations suggest that the detection limit for Sb under the current measurement conditions lies not far below 5 nm thickness.

Despite fixed beam parameters, the total signal intensity fluctuated between measurements. This is likely due to instability in the cold field emitter or changes in surface charging after each deposition, both of which can affect the local beam current or electron focusing conditions.

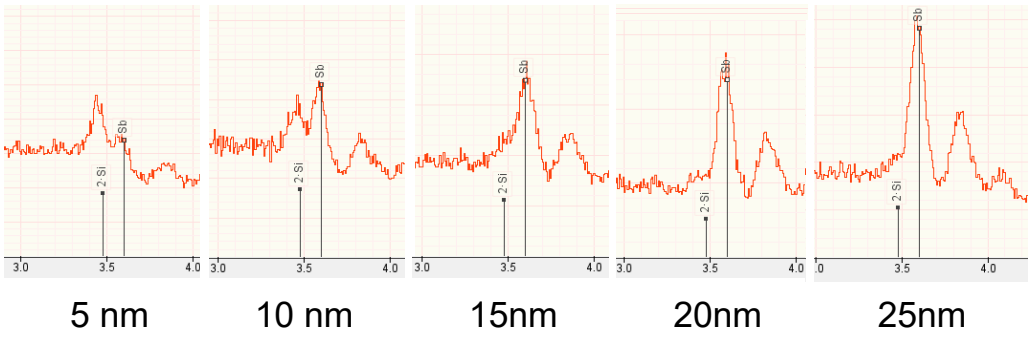

Figure 4.11: *Region of the Sb L_α peak in the spectra of the Sb-on-SiN series, with Sb thickness increasing from 5 to 25 nm. The spectra are summed over two scans and offset for clarity. Markers indicate the Si sum peak and Sb L_α peak positions.*

To quantify this trend, the height of the Sb L_α peak was normalized to the corresponding Si K_α peak in each spectrum. These ratios were then normalized to the value measured in the 5 nm sample (1/1294), which was set to 1. The results are listed in Table 4.12. While these ratios do not represent absolute intensities, they offer a consistent reference across the series that compensates for the inconsistent electron dose. The peak intensities were extracted after background subtraction using the Clayton algorithm.

Thickness (nm)	Normalized Sb L_α / Si K_α Ratio
5	1.0
10	2.3
15	4.1
20	5.4
25	6.9

Figure 4.12: *Normalized Sb L_α to Si K_α peak ratios for Sb-on-SiN samples of varying thickness. The ratio is normalized to 1 at 5 nm and increases with Sb film thickness.*

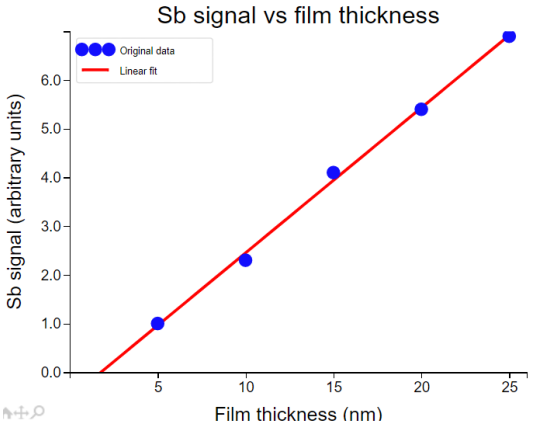

Figure 4.13: *Linear fit to the measured data, indicating that the Sb signal detection limit lies slightly below a film thickness of 5 nm.*

These results confirm that the EDX system can detect sub-10 nm Sb layers on a silicon-based substrate. From 10 nm upward, the Sb signal becomes

strong enough for reliable peak fitting and, therefore, quantitative analysis. The actual detection threshold may vary depending on the element of interest or the substrate material, as the Si sum peak can interfere with low-intensity Sb L_α signals. Spectra could also be improved by extending the acquisition time, the spectra in Figure 4.11 represent just 360 seconds of total measurement. Longer acquisition or averaging would further improve signal-to-noise and accuracy near the detection limit.

This thickness series provides a useful reference for interpreting the Cs_3Sb measurements discussed earlier. In particular, the limited Sb visibility in the thinnest Cs_3Sb samples can now be understood as falling near or just below the EDX detection threshold. The clear emergence of Sb peaks from 10 nm onward also supports the results observed in the third Cs_3Sb sample, where a 25 nm film yielded reliable stoichiometry estimates in both MLLSQ and DTSA-II analysis. Thus, the Sb-on-SiN spectra provide a practical baseline for understanding and affirming EDX sensitivity limits in real photocathode samples.

Chapter 5

Discussion

5.1 Implications for Photocathode Growth

The results of this project show that EDX analysis in the LEEM system can provide meaningful insights into the composition of in-situ grown Cs_3Sb photocathodes. While the measured stoichiometries deviate from the ideal 3:1 Cs:Sb ratio, the observed trend of stronger signals and more realistic ratios in thicker films is in line with expectations. The thicker photocathode sample exhibited clear antimony peaks and a stoichiometry closer to the ideal, suggesting that the films are indeed near optimal composition. However, the very low antimony levels in these thin films push the detection limits of the system.

The measurements on the antimony thin film series further showed that at film thicknesses below about 5 nm, the antimony Lα peak becomes very difficult to distinguish from the silicon sum peak of the substrate. Considering that a Cs_3Sb photocathode with a thickness of 12 to 15 nm and an expected 1:3 antimony-to-cesium ratio contains an effective antimony thickness well below 5 nm. This explains why the first and second photocathode samples produced ratios with unrealistically high Cs:Sb ratios due to nearly undetectable antimony. In these thin samples, the software was unable to properly fit the antimony peak when it is merged with the silicon sum peak, which dramatically increases the antimony concentration uncertainty levels. This limitation highlights the need for further optimization if stoichiometric analysis of very thin photocathodes is to be performed accurately in this setup, by either reducing the Si sum peak or increasing photocathode cathodoluminescence.

Version of August 27, 2025– Created August 27, 2025 - 11:10

5.2 Accuracy and Limitations of the Measurement Approach

The accuracy and reliability of the stoichiometric analysis in this work were limited by several factors. First, the LEEM's cold field emitter was in a suboptimal condition during the measurements. The pressure in the electron gun was observed to fall into the 10^{-10} mbar range, indicating contamination in the gun and on the emitter tip. As a consequence, the emission current fluctuated significantly between measurement days, sometimes by as much as 50%. Making the exact beam current an unknown, preventing accurate quantification of absolute signal intensities, and limiting the analysis to relative peak comparisons.

Another major limitation was the absence of a reliable method to directly measure the beam current reaching the sample during EDX acquisition. The system lacked a Faraday cup or any equivalent means of measuring the current at the sample position. In practice, an approximate value of 1 nA was assumed and provided to DTSA-II for all calculations and simulations. However, other experimental parameters, such as the exact sample-to-lens distance, could not be verified, as this distance had often changed to obtain a higher signal, therefore, an average distance of 3.5nm was provided in DTSA-II. As a result, the stoichiometric analysis was effectively reduced to a comparison of relative peak intensities, without a reliable determination of absolute compositions.

If the beam current at the sample could be measured directly and reproducibly, it would become possible to relate the measured X-ray signal to absolute properties, such as the thickness of the photocathode layer. This would be particularly useful for analyzing film samples, where the composition and thickness of a thin film on a bulk substrate must be determined simultaneously. To achieve this, however, a thin-film cesium standard would also be required. Such a standard would enable the application of the ζ-factor method, which is specifically designed for thin-film quantification. Producing a reliable thin-film cesium standard could be recommended for future experiments, as it would allow for a more robust and physically meaningful analysis of photocathode samples.

Version of August 27, 2025– Created August 27, 2025 - 11:10

Chapter 6

Conclusion

This thesis evaluated the capabilities of the EDX system integrated into the ESCHER LEEM for compositional analysis of in-situ grown Cs_3Sb photocathodes, focusing on its detection limits and suitability for the group's ONEM research.

Calibration standards, matrix-corrected spectrum fitting, and Monte Carlo simulations were applied to analyze photocathodes of varying thickness. The results showed that the system can provide meaningful stoichiometric information, but becomes unreliable when the sample thickness is too low. In typical Cs_3Sb photocathodes of around 10-20 nm, the antimony content is insufficient for reliable compositional analysis. Thicker films showed more distinct antimony and cesium peaks, with measured ratios closer to the nominal 3:1 stoichiometry.

The study also highlighted key limitations of the setup. The cold field emitter exhibited unstable emission currents, and the lack of a direct beam current measurement at the sample hindered absolute quantification and comparison with simulations.

Overall, this work provides a clear assessment of what the LEEM-EDX system can and cannot currently achieve for photocathode characterization. It enables qualitative and relative analysis when sufficient material is present, but further improvements are required for accurate quantitative measurements. Recommended next steps include emitter maintenance, implementing beam current monitoring at the sample, and developing a thin-film cesium standard to allow advanced methods such as ζ-factor quantification.

Version of August 27, 2025– Created August 27, 2025 - 11:10

Acknowledgements

I would like to express my gratitude to everyone who supported me during this thesis project. First, I would like to thank my supervisor, Prof. dr. ir. S. J. van der Molen, for allowing me to work on this project within the Van der Molen Lab and for providing guidance and feedback throughout the process. I am grateful to the members of the lab for creating such a friendly and collaborative environment. I especially want to thank Guido, Noud, and Esra for being approachable and helpful whenever I had questions and for the help in the lab, whether it was aligning the gun, troubleshooting the setup, or just having a chat. Hugo also deserves special thanks for working alongside me during the photocathode and thin film measurements. As his project fabricating high QE photocathodes directly complemented my work with the EDX, and it was fun to be able to work together in the lab. Finally, I would like to thank the entire Van der Molen group for the pleasant and welcoming atmosphere. The morning coffee and lunch breaks were often a highlight of the day in between the serious work. Working on this project has been a rewarding experience, and I'm glad I could contribute to the ongoing research in the group. Thank you all for making it an enjoyable time.

Bibliography

[1] FAST SDD Ultra High Performance Silicon Drift Detector.

[2] Apr 2025.

[3] E. Acosta, X. Llovet, and F. Salvat. Monte carlo simulation of bremsstrahlung emission by electrons. *Applied Physics Letters*, 80(17):3228–3230, 04 2002.

[4] H. A. Kramers and. Xciii. on the theory of x-ray absorption and of the continuous x-ray spectrum. *The London, Edinburgh, and Dublin Philosophical Magazine and Journal of Science*, 46(275):836–871, 1923.

[5] Ulrich Wolfgang Arndt, W. A. Coates, and A. R. Crathorn. A gas-flow x-ray diffraction counter, 1954.

[6] Microscopy Australia. `https://myscope.training/`.

[7] Johannes Bernardi. *Energy-dispersive X-ray spectroscopy*. 05 2021.

[8] David Bote and Francesc Salvat. Calculations of inner-shell ionization by electron impact with the distorted-wave and plane-wave born approximations. *Phys. Rev. A*, 77:042701, Apr 2008.

[9] Harry R. Bowman, Earl K. Hyde, Stanley G. Thompson, and Richard C. Jared. Application of high-resolution semiconductor detectors in x-ray emission spectrography. *Science*, 151(3710):562–568, 1966.

[10] Benton C Clark III, AK Baird, Harry J Rose Jr, Priestley Toulmin III, Ralph P Christian, Warren C Kelliher, Angelo J Castro, Catherine D

Rowe, Klaus Keil, and Gary R Huss. The viking x ray fluorescence experiment: Analytical methods and early results. *Journal of Geophysical Research*, 82(28):4577–4594, 1977.

[11] Ray Fitzgerald, Klaus Keil, and Kurt FJ Heinrich. Solid-state energy-dispersion spectrometer for electron-microprobe x-ray analysis. *Science*, 159(3814):528–530, 1968.

[12] Oxford Instruments. Silicon drift detectors explained.

[13] JEOL. `https://www.jeol.com/words/semterms/20121024.062458.php#gsc.tab=0`.

[14] Jeffrey B Kortright. X-ray data booklet.

[15] Yougui Liao. *Practical Electron Microscopy and Database: www.globalsino.com/EM/*. GlobalSino, 02 2013.

[16] Gaurav Mishra, Anil Kumar Mandariya, S.N. Tripathi, Mariam, Manish Joshi, Arshad Khan, and B.K. Sapra. Hygroscopic growth of csi and csoh particles in context of nuclear reactor accident research. *Journal of Aerosol Science*, 132:60–69, 2019.

[17] Dale E Newbury and Nicholas W M Ritchie. Energy-Dispersive X-Ray Spectrum Simulation with NIST DTSA-II: Comparing Simulated and Measured Electron-Excited Spectra. *Microscopy and Microanalysis*, 28(6):1905–1916, 9 2022.

[18] J-L Pouchou and F Pichoir. Les éléments très légers en microanalyse x. possibilités des modèles récents de quantification. *Journal de microscopie et de spectroscopie électroniques*, 11(4):229–250, 1986.

[19] Joshua Schaafsma. edx-in-leem. Master's thesis, Leiden Universiteit, July 2024.

[20] Craig Schwandt. Low voltage microanalysis, May 2022.

[21] Stephen Seltzer. Tables of x-ray mass attenuation coefficients and mass energy-absorption coefficients, NIST standard reference database 126, 1995.

[22] Francesco Sgaramella, M Miliucci, Massimiliano Bazzi, Damir Bosnar, Mario Bragadireanu, Marco Carminati, M Cargnelli,

A Clozza, Griseld Deda, L. Paolis, R Grande, Carlo Fiorini, C Guaraldo, M. Iliescu, Masahiko Iwasaki, Pietro King, P. Levi Sandri, Johann Marton, Pawel Moskal, and C Curceanu. The siddharta-2 calibration method for high precision kaonic atoms x-ray spectroscopy measurements. *Physica Scripta*, 97, 10 2022.

[23] Wouter Guido Stam. *Optical near-field electron microscopy: merging light and electron imaging*. PhD thesis, Universiteit Leiden, 2025.

[24] Keith Thompson. "https://assets.thermofisher.com/TFS-Assets/CAD/Warranties/TN52342$_{E0}$512$M_Silicon Drift_H$.pdf".

[25] R.M. Tromp, J.B. Hannon, A.W. Ellis, W. Wan, A. Berghaus, and O. Schaff. A new aberration-corrected, energy-filtered leem/peem instrument. i. principles and design. *Ultramicroscopy*, 110(7):852–861, 2010.

[26] Rudolf M. Tromp. Energy-dispersive x-ray spectroscopy in a low energy electron microscope. *Ultramicroscopy*, 259:113935, 2024.

[27] Kartik Venkatraman and Peter A. Crozier. Role of convergence and collection angles in the excitation of long- and short-wavelength phonons with vibrational electron energy-loss spectroscopy. *Microscopy and Microanalysis*, 27(5):1069â1077, June 2021.